OXFORD

Research Article

A photoactivatable and phenylboronic acid-functionalized nanoassembly for combating multidrug-resistant gram-negative bacteria and their biofilms

Xiaoqing Zhou[1,†], Lanlan Dong[2,†], Baohua Zhao[2], Guangyun Hu[2], Can Huang[2], Tengfei Liu[3], Yifei Lu[2], Mengxue Zheng[1], Yanlan Yu[1], Zengjun Yang[1], Shaowen Cheng[4], Yan Xiong [5], Gaoxing Luo[2], Wei Qian [2,*] and Rui Yin [1,*]

[1]Department of Dermatology, Southwest Hospital, Army Medical University (Third Military Medical University), No. 29 Gaotanyan Road, Shapingba District, Chongqing 400038, China, [2]Institute of Burn Research, State Key Laboratory of Trauma, Burn and Combined Injury, Key Laboratory of Disease Proteomics of Chongqing, Southwest Hospital, Army Medical University (Third Military Medical University), No. 29 Gaotanyan Road, Shapingba District, Chongqing 400038, China, [3]Department of Burn and Plastic Sugery, No. 906 Hospital of Joint Logistic Support Force of PLA, No. 377 Zhongshan East Road, Yinzhou District, Ningbo 315100, China, [4]Department of Wound Repair, the First Affiliated Hospital of Hainan Medical University, No. 31 Longhua Road, Haikou 570102, China and [5]Department of Orthopaedics, Daping Hospital, Army Medical University (Third Military Medical University), No. 10 Changjiang Branch Road, Yuzhong District, Chongqing 400042, China

*Correspondence: Wei Qian, Email: weiqian87@126.com; Rui Yin, Email: swyinrui@163.com
†Xiaoqing Zhou and Lanlan Dong contributed equally.

Abstract

Background: Multidrug-resistant (MDR) gram-negative bacteria-related infectious diseases have caused an increase in the public health burden and mortality. Moreover, the formation of biofilms makes these bacteria difficult to control. Therefore, developing novel interventions to combat MDR gram-negative bacteria and their biofilms-related infections are urgently needed. The purpose of this study was to develop a multifunctional nanoassembly (IRNB) based on IR-780 and N, N′-di-sec-butyl-N, N′- dinitroso-1,4-phenylenediamine (BNN6) for synergistic effect on the infected wounds and subcutaneous abscesses caused by gram-negative bacteria.
Methods: The characterization and bacteria-targeting ability of IRNB were investigated. The bactericidal efficacy of IRNB against gram-negative bacteria and their biofilms was demonstrated by crystal violet staining assay, plate counting method and live/dead staining *in vitro*. The antibacterial efficiency of IRNB was examined on a subcutaneous abscess and cutaneous infected wound model *in vivo*. A cell counting kit-8 assay, Calcein/PI cytotoxicity assay, hemolysis assay and intravenous injection assay were performed to detect the biocompatibility of IRNB *in vitro* and *in vivo*.
Results: Herein, we successfully developed a multifunctional nanoassembly IRNB based on IR-780 and BNN6 for synergistic photothermal therapy (PTT), photodynamic therapy (PDT) and nitric oxide (NO) effect triggered by an 808 nm laser. This nanoassembly could accumulate specifically at the infected sites of MDR gram-negative bacteria and their biofilms via the covalent coupling effect. Upon irradiation with an 808 nm laser, IRNB was activated and produced both reactive

oxygen species (ROS) and hyperthermia. The local hyperthermia could induce NO generation, which further reacted with ROS to generate $ONOO^-$, leading to the enhancement of bactericidal efficacy. Furthermore, NO and $ONOO^-$ could disrupt the cell membrane, which converts bacteria to an extremely susceptible state and further enhances the photothermal effect. In this study, IRNB showed a superior photothermal-photodynamic-chemo (NO) synergistic therapeutic effect on the infected wounds and subcutaneous abscesses caused by gram-negative bacteria. This resulted in effective control of associated infections, relief of inflammation, promotion of re-epithelization and collagen deposition, and regulation of angiogenesis during wound healing. Moreover, IRNB exhibited excellent biocompatibility, both *in vitro* and *in vivo*.

Conclusions: The present research suggests that IRNB can be considered a promising alternative for treating infections caused by MDR gram-negative bacteria and their biofilms.

Key words: Photothermal therapy, Photodynamic therapy, Nitric oxide, Synergistic, Boronic acid, Multidrug-resistant gram-negative bacteria

Highlights

- IRNB showed a superior photothermal-photodynamic-chemo synergistic effect on the infected wounds and subcutaneous abscesses caused by gram-negative bacteria.
- IRNB could specifically accumulate at the infected sites of MDR gram-negative bacteria and their biofilms, enhancing bactericidal efficacy and decreasing side effects to surrounding healthy tissues.

Background

Bacterial infection-related diseases pose a significant public health burden that increases healthcare expenditures and mortality. Studies of inpatient data revealed that multidrug-resistant (MDR) gram-negative bacteria, including *Pseudomonas aeruginosa* (*Pa*), *Acinetobacter baumannii* (*Ab*) and *Klebsiella pneumoniae* (*Kp*), are listed as urgent and severe threats [1–4]. These pathogens are intrinsically resistant to most available antibiotics, making the treatment challenging. Drug resistance evolves primarily because of the selection pressures imposed by antibiotics for the treatment of the targeted pathogens and bacterial biofilms [5,6]. Spatially structured biofilms are heterogeneous bacterial aggregates, and can survive in various unfavorable conditions compared with planktonic bacteria. Moreover, the formation of biofilms is a significant contributor in approximately 80% of all bacterial infections, including chronic infected wounds, such as cystic fibrosis, endocarditis, osteomyelitis, Crohn's disease and the development of some cancers [7,8]. Therefore, it is crucial to develop novel interventions for combating MDR gram-negative bacteria and their biofilms.

Recently, phototherapy has been considered as an innovative and promising strategy to combat MDR bacterial infections, which includes photodynamic therapy (PDT) and photothermal therapy (PTT) [9–13]. In PDT, photosensitizers can produce reactive oxygen species (ROS) under irradiation at a specific wavelength. In PTT, photothermal agents can generate localized hyperthermia with laser illumination. ROS generated by PDT could damage most biomacromolecules, such as proteins, lipids and nucleic acids and kill cells and demonstrated its killing efficacy against various bacteria, fungi and viruses [14–17]. Similarly, the elevated

temperatures generated by PTT could prompt bacterial protein denaturation, crosslinking of DNA, disruption of the bacterial cell membrane and ablation of biofilms [18,19]. A growing tendency has also been emerging that a combination of PDT and PTT could trigger the simultaneous production of hyperthermia and ROS upon laser irradiation, and thus exert synergistic effects resulting in the inactivation of bacteria. So far, various phototherapeutic nanomaterials for bactericidal applications, including pyridyl-porphine-based nanoparticles [20], phenothiazine dye-based nanoparticles [21], carbon-based nanomaterials [22], metal nanomaterials [23] and polymeric nanomaterials [24] have been investigated. Of these, heptamethine cyanine dyes (e.g. indocyanine green, IR-780, IR-808 and IR-825) have attracted increasing interest based on the integration of PDT, PTT and fluorescence imaging [25,26]. Notably, IR-780, a typical heptamethine cyanine dye, has strong absorption properties in the near infrared (NIR) spectrum and generates thermal and $^1O_2$ upon NIR laser radiation, thereby demonstrating the ideal PDT/PTT efficacy [27]. Moreover, IR-780 promptly emits fluorescence following illumination, exhibiting its excellent *in vivo* fluorescence imaging ability [28]. Nevertheless, the major limitation of IR-780–based antibacterial PTTs/PDTs is that the insufficient specificity of the phototherapeutic agents toward pathogenic cells or infected sites may damage healthy tissues. High heat may also induce undesirable inflammation via excessive heat diffusion. Furthermore, monotherapy is far less effective for MDR bacteria and biofilm infections than combination therapies [29]. Therefore, there is an urgent need to develop target-specific nanoplatforms and synergistic therapies to reduce side effects and optimize treatment efficacy.

In recent years, physiologically active gases, such as nitric oxide (NO), carbon monoxide, sulfur dioxide, hydrogen sulfide and hydrogen have drawn increasing attention for antibacterial applications [30–34]. The ultrasmall gas molecules can freely permeate biological membranes and exert their therapeutic effects. Among them, NO has been the most extensively investigated antibacterial agent. NO is an endogenously produced gaseous molecule that induces cell damage at high concentrations (>1 μM) [35,36] and regulates normal physiological processes at low concentrations ($\approx$nM) [37–39]. Moreover, its derivatives containing nitrite and nitrate ions exert antimicrobial properties via nitrosative and oxidative stress, contributing to the disruption of fundamental cellular functions or structures [35]. Additionally, NO can react with ROS to generate reactive nitrogen species (RNS), including peroxynitrous acid and the peroxynitrite anion $ONOO^-$ [40], which exhibit a stronger bactericidal activity than ROS by virtue of free radical peroxidation [41,42]. Particularly, NO stimulates wound healing by facilitating the de-adhesion and proliferation of epidermal stem cells as well as enhancing myofibroblast and collagen production [43]. Therefore, combining NO with phototherapy may enhance the bactericidal efficiency with additional benefits. In comparison with short-wavelength laser, NIR laser (780–1100 nm) achieves deeper tissue penetration and causes less damage on ambient normal tissues [44]. However, the development of new NIR-laser-triggered NO-releasing platforms is still in its initial stages.

Boronic acid (BA) is composed of a boron center and three hydroxyl groups, which can bind to diol-containing saccharides by forming covalent boronic esters. As the cell wall of gram-negative bacteria and biofilm matrix are rich in diol-containing polysaccharides, BA and its derivatives have been utilized as specific targeting components in antibacterial nanomaterials [45,46]. Until now, the aforementioned unique targeting ability, low toxicity, stability and ease of assembly have made BA and its derivatives appealing for the development of bactericidal materials.

Based on all the above considerations, we developed a new nanoassembly with the NIR dye IR-780 and the heat-sensitive NO donor N, N'-di-sec-butyl-N, N'- dinitroso-1,4-phenylenediamine (BNN6). These were further modified with lecithin and DSPE-PEG-phenylboronic acid (PBA) on the nanoassembly surface (Figure 1a). As shown in Figure 1b, the constructed IR-780/BNN6-PEG-PBA (IRNB) can selectively bind to the cell walls of gram-negative bacteria and the biofilm matrix. The B-OH bonds of PBA ligand can target bacterial polysaccharides and form covalent boronic esters. This effect can significantly enhance bactericidal efficiency and decrease side effects to surrounding healthy tissues. Upon illumination with the 808 nm NIR laser, IRNB can release ROS and induce hyperthermia that subsequently induces controlled NO release. NO can react with ROS to produce RNS, thereby enhancing the efficiency of PDT. Furthermore, ROS and NO can also destroy the integrity of the bacterial cell membrane, leading to a heat-sensitive bacterial phase, which will further enhance the photothermal effect. Furthermore, the fluorescent and photothermal properties of IR-780 make IRNB favorable for fluorescent and thermal imaging of infected tissues. The present study aims to investigate the PTT, PDT and NO effects, the bacteria-targeting ability and the PTT/PDT/NO synergistic antibacterial effect against MDR gram-negative *Pa*, *Kp* and *Ab*, as well as eradication effects on bacterial biofilms both *in vitro* and *in vivo*.

Methods

Materials

IR-780 iodide was purchased from J&K Scientific Ltd (Beijing, China). BNN6 was synthesized by Shanghai Nayuansu Biochemical Technology Co., Ltd (Shanghai, China). Lecithin and 1,2-distearoyl-sn-glycero-3-phosphoethanolamine-N-[methoxy (polyethylene glycol)-2000] (DSPE-PEG-2000) were purchased from Xian Ruixi Biochemical Technology Co., Ltd (Xian, China). 1,2-Distearoyl-sn-glycero-3-phosphoethanolamine-N-[methoxy (polyethylene glycol)-2000]-phenylboronic acid (DSPE-PEG-PBA) was synthesized by Xi'an Qiyue Biochemical Technology Co., Ltd (Xi'an, China). 1,3-Diphenylisobenzofuran (DPBF), 2′,7'-Dichlorodihydrofluorescein diacetate (DCFH-DA) and Dihydrorhodamine 123 (DHR 123) were purchased from MedChem Express, LLC (Shanghai, China). The Griess assay kit and Calcein/PI cytotoxicity assay kit were purchased from Beyotime Biotechnology Co. (Shanghai, China). 4-Amino-5-methylamino-2′,7′-difluorofluorescein diacetate (DAF-FM DA) and rabbit monoclonal antibody platelet endothelial cell adhesion molecule-1 (CD31) were purchased from Abcam (Cambridge, UK). The SYTO9/PI live/dead bacterial and biofilm viability kit was purchased from Invitrogen (Carlsbad, CA, USA). The crystal violet (CV) dye was purchased from Sigma (St. Louis, MO, USA). A Cell Counting Kit-8 (CCK-8) and modified Masson's trichrome stain kit were purchased from Beijing Solarbio Science & Technology Co., Ltd (Beijing, China). Rabbit monoclonal antibody interleukin-6 (IL-6), rabbit mAb tumor necrosis factor (TNF)-α, anti-rabbit IgG (H + L) and F (ab')2 Fragment (Alexa Fluor® 647 Conjugate) were purchased from Cell Signaling Technology (Danvers, MA, USA). MDR *Ab*, *Kp* and *Pa* samples were clinical isolates sourced from the Institute of Burn Research, Southwest Hospital, Army Medical University (Chongqing, China). Luria–Bertani (LB) agar was purchased from Hopebiol Co., Ltd (Qingdao, China). Dulbecco's Modified Eagle Medium (DMEM, high glucose) and fetal bovine serum (FBS) were purchased from Gibco (New York, USA). NIH 3 T3 fibroblast cells were provided by the Chinese Academy of Sciences (Shanghai, China). BALB/c mice (male, 20–25 g, 6–8 weeks) were obtained from the Experimental Animal Department of the Army Medical University. All the animal experiments complied with the ethical principle of the Institutional Animal Care and Use Committee of the Army Medical University.
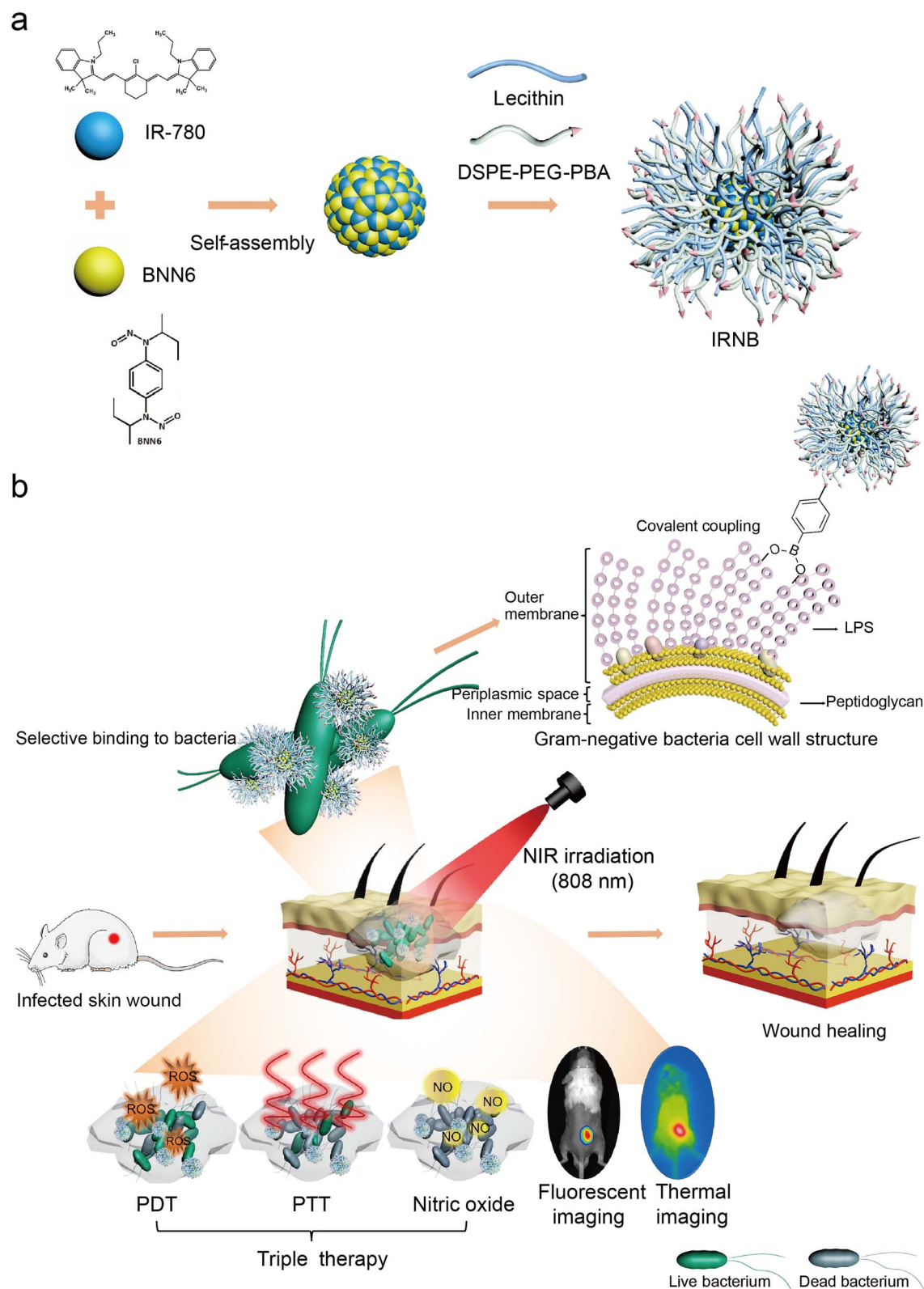
Figure 1. Schematic diagram of the preparation and antimicrobial mechanism of IRNB. (**a**) Schematic illustration of the preparation of IRNB. (**b**) The antimicrobial mechanism of IRNB *in vivo*. *IRNB* IR-780/BNN6-PEG-PBA, BNN6 N,N′-di-sec-butyl-N,N′-dinitroso-1,4-phenylenediamine, *DSPE-PEG-PBA* 1,2-distearoyl-snglycero-3-phosphoethanolamine-N-[methoxy(polyethylene glycol)-2000]-phenylboronic acid, *LPS* lipopolysaccharide, *NIR* near infrared laser, *PDT* photodynamic therapy, *PTT* photothermal therapy

Preparation of IR-780-PEG NPs, BNN6-PEG NPs and IR-780-BNN6-PEG NPs (IRN)

To prepare NPs, we dissolved 5 mg IR-780 iodide in 1 mL acetonitrile (CH_3CN) solution. Lecithin and DSPE-PEG-2000 (200uL, 20 mg/mL in ethanol) were then dissolved in 6 mL deionized water (DI water) and stirred at 1200 rpm for 30 min at 60°C. The IR-780 iodide/CH_3CN solution was then dripped into 6 mL of the preheated solution, and the solution was stirred at 1200 rpm for 2 h at 25°C. The original IR-780-PEG NP suspension was centrifuged at 3000 rpm for 10 min, then dialyzed with an 8 kDa molecular weight cut-off (MWCO) dialysis bag for 4 h in DI water to remove CH_3CN, free IR-780, free lecithin and DSPE-PEG-2000. The remaining solution contained the successfully synthesized IR-780-PEG NPs. The BNN6-PEG and IR-780-BNN6-PEG NPs were also prepared by this method.

Preparation of IR-780-BNN6-PEG-PBA NPs (IRNB)

To prepare the IR-780-BNN6-PEG-PBA NPs, we first dissolved 5 mg IR-780 iodide and 5 mg BNN6 in 1 mL CH_3CN solution. Lecithin and DSPE-PEG-PBA (200uL, 20 mg/mL in ethanol) were dissolved in 6 mL DI water and stirred at 1200 rpm for 30 min at 60°C. The IR-780 iodide/BNN6/CH_3CN solution was then dripped into 6 mL of the preheated solution, which was stirred at 1200 rpm for 2 h at 25°C. The original IR-780-BNN6-PEG-PBA NP suspension was centrifuged at 3000 rpm for 10 min then dialyzed with 8 kDa MWCO dialysis bag for 4 h in DI water to remove CH_3CN, free IR-780, free BNN6, free lecithin and DSPE-PEG-PBA, and IR-780-BNN6-PEG-PBA NPs were successfully synthesized.

Characterization

The sizes and morphologies of IR-780-PEG NPs, BNN6-PEG NPs, IRN and IRNB were determined using hydrodynamic particle sizing (Zetasizer Nano ZEN5600, Malvern Instruments, UK) and transmission electron microscopy (TEM) using the JEOL JEM-1400 TEM analyzer, Japan, respectively. UV–Vis and fluorescence spectra were analyzed by a spectrophotometer (UV-3600, Shimadzu, Japan). Finally, Fourier transform infrared (FTIR) spectra between 400 and 4000 cm^{-1} were recorded using a Nicolet 6700 FTIR instrument (Thermo Fisher, USA). The hydrodynamic stability of IRNB was investigated after incubation with DI water, phosphate-buffered saline (PBS) and PBS containing 10% FBS at 4°C for 7 days. The variation in hydrodynamic diameter was recorded by a particle sizing instrument.

Release profiles of IRNB

IRNB nanoassembly (5 mL, 2 mg/mL) were dialyzed against 200 mL PBS at 37°C with NIR laser or kept in the dark with constant shaking at 250 rpm. For a specific time period, 2 mL of the dialysis solution was removed and 2 mL of fresh PBS was added. The concentrations of IR-780 and BNN6 were analyzed by a UV–Vis spectrophotometer at 786 nm and 367 nm, respectively.

Photothermal properties of IRNB

The photothermal effect of IRNB was measured and analyzed under the illumination of an NIR laser (808 nm, 0.5–1.0 W/cm^2, 0–660 s). The photothermal effects of IRNB at various concentrations (0, 50, 100 and 250 μg/mL) and at various power densities (0.5, 0.75 and 1 W/cm^2) were investigated. The temperature was documented at 30 s intervals using a digital thermometer. Next, temperature curves were plotted, followed by the calculation of photothermal conversion efficiency (η) to assess the photothermal stability of IRNB. The photothermal stability of IRNB was investigated with repeated on/off NIR laser illumination cycles. IRNB was illuminated with five successive laser cycles (100 μg/mL, 0.75W/cm^2, 10 min on and 10 min off). The temperature was documented at 30 s intervals using a digital thermometer.

Detection of ROS, NO and ONOO generation of IRNB

DPBF, a Griess assay kit, and DHR 123 were used to detect IRNB generation of ROS, NO and $ONOO^-$, respectively, following laser illumination. IRNB was illuminated with an NIR laser (808 nm, 0.75 W/cm^2) for a specific time period, and DPBF/Griess reagent/DHR 123 were added to the aqueous solution. Absorbances were then measured at 410 nm, 540 nm and 525 nm, respectively.

Detection of intracellular ROS and NO

DCFH-DA and DAF-FM DA were utilized to demonstrate the ROS- and NO-releasing properties of IRNB in MDR *Ab*, *Kp* and *Pa* cells, respectively. First, *Ab*, *Kp* and *Pa* bacterial suspensions (1×10^8 CFU/mL) were treated with PBS, BNN6-PEG, IR-780-PEG, IRN and IRNB for 30 min at 37°C, respectively. To completely remove free nanomaterials, the resulting suspensions were centrifuged (6000 rpm, 5 min) and rinsed three times with sterile PBS. Next, the sediments were resuspended in 1 mL PBS following irradiation with an 808 nm NIR laser (0.75 W/cm^2, 10 min). Then, DCFH-DA and DAF-FM DA were used to stain bacteria following the manufacturer's instructions. Finally, the bacteria were observed through a confocal laser scanning microscope (CLSM; Olympus Corporation, Tokyo 163–0914, Japan). The intracellular ROS was quantitatively measured based on previous studies [47]. The resulting bacteria suspensions were diluted to the concentration of 10^6 CFU/mL and the fluorescence emission spectra were recorded by a fluorophotometer (LS-55, Perkin Elmer, USA, excitation wavelength: 488 nm). Bacteria suspensions were treated with 4 mM H_2O_2 and PBS to set as the positive and negative control. The photomultiplier tube voltage was 700V.

Culture of bacteria and their biofilms

MDR *Ab*, *Kp* and *Pa* were cultured in 4 mL Luria–Bertani (LB) broth (Hopebiol, Qingdao, China) and shaken at 230 rpm at 37°C overnight. The resultant bacteria—in the logarithmic phase—were then centrifuged (6000 rpm,

5 min) and washed three times with sterile PBS. The bacterial sediments were then resuspended in PBS. The optical densities were measured at a wavelength of 600 nm using a spectrophotometer (SmartSpec 30, Bio-Rad, California, USA) to adjust the bacterial concentration to 1×10^8 CFU/mL.

A total of 100 μL LB medium and 10 μL bacterial suspension in the logarithmic phase with an OD600 of 0.5 were added to a 96-well plate. The plate was incubated at 37°C. After 12 h, LB medium was carefully and gently removed, and fresh LB medium was added. After 48 h, LB medium was removed and the biofilms were carefully rinsed three times with sterile PBS to wash off the suspended bacteria. Thereafter, biofilms at the bottom of the well were harvested.

Interactions between IRNB and bacteria *in vitro*

The bacteria-targeting ability of IRNB was assessed using the infrared thermographic camera and scanning electron microscope (SEM). Briefly, 900 μL of bacterial solution (10^8 CFU/mL) was coincubated with 100 μL of prepared BNN6-PEG/IR-780-PEG/IRN/IRNB (1 mg/mL) under dark conditions at 37°C for 30 min, respectively. Next, the bacterial solutions were centrifuged (6000 rpm, 5 min) and rinsed three times with sterile PBS to remove free nanomaterials. Then, the pellet was resuspended in 1 mL PBS following illumination with an NIR laser (808 nm, 0.75 W/cm², 10 min). An infrared camera (FLIR-E49001, Estonia) was used to determine the temperature with an accuracy of 0.1°C. Subsequently, SEM (Crossbeam 340, Zeiss, Germany) was used for recognizing bacterial morphological alterations. Following bacteria incubation with the nanomaterials, washing and resuspension in PBS, 10 μL bacterial solution was dropped onto a cell climbing slice. Then, 2.5% glutaraldehyde was used to fix the product overnight at 4°C. Next day, the specimens were rinsed with sterile saline for 10 min and dehydrated in a sequence of ethanol solutions (30%, 50%, 70%, 95% and 100%) ending with tert-butanol. After gold spray treatment, bacterial products were viewed using SEM.

Antibacterial experiments *in vitro*

The plate counting method, live/dead staining and TEM morphological observation were utilized for antibacterial testing. Initially, 900 μL bacterial solution (OD 0.5) were coincubated with 100 μL of prepared PBS/BNN6-PEG/IR-780-PEG/IRN/IRNB (1 mg/mL) under dark conditions at 37°C for 30 min, respectively. Next, the bacterial suspensions were centrifuged (6000 rpm, 5 min) and rinsed three times with sterile PBS to wash off free nanomaterials. The pellets were then resuspended in 1 mL PBS following illumination by an NIR laser (808 nm, 0.75 W/cm², 10 min). Groups without NIR laser irradiation were set as controls.

For the plate counting method, the bacterial solution was sequentially diluted, then 50 μL of the resultant bacterial solution was smeared evenly on a nutrient agar plate. After growth for 18 h in a 37°C incubator, colonies were calculated and photographed with an automatic colony enumeration instrument (Supcre, Shineso, Hangzhou) [48].

For live/dead staining, the bacterial solution was centrifuged (6000 rpm, 5 min) and resuspended in 1 mL sterile PBS. Then, 1 μL STYO9 and 1 μL PI (live/dead staining kit, Invitrogen, USA) was used to stain bacteria and then kept in the dark for 15 min. Thereafter, bacteria were rinsed and resuspended in 1 mL PBS. Next, 10 μL bacterial suspension was added dropwise onto a glass slide. The prepared slides were viewed under a research slide scanner (SLIDEVIEW VS200, Olympus).

For TEM morphological observation of the bacteria, bacterial solutions were centrifuged (6000 rpm, 5 min) then rinsed with 1 mL sterile PBS, after which the bacterial suspensions were centrifuged (10 000 rpm, 10 min). Next, the PBS supernatant was carefully blotted off and replaced with 1 mL 2.5% glutaraldehyde and left overnight. The fixed bacteria were rinsed three times with sterile PBS for 15 min and fixed with osmic acid for 2 h. Then, the specimens were washed three times with sterile PBS for 15 min following dehydration in a sequence of graded acetone (50, 70, 90 and 100%) and then transferred to epoxy resin solutions for 3–4 h (acetone/epoxy resin = 1/1, v/v, 500 μL). Subsequently, the samples were embedded in resin solution for 4 h and cured in a resin embedding module for 48 h. Finally, cured samples were sectioned into 70 nm-thick slides and placed on copper grids for TEM observation.

Anti-biofilm experiments *in vitro*

After the biofilms were formed and washed with PBS, 100 μL PBS/BNN6-PEG/IR-780-PEG/IRN/IRNB were coincubated with biofilms for 30 min at 37°C, respectively. The biofilms were then rinsed three times with PBS and illuminated with an NIR laser (808 nm, 0.75 W/cm², 10 min). The groups incubated with PBS/nanomaterials without NIR laser irradiation were set as controls.

For crystal violet (CV) staining assay, the biofilms were fixed with methanol (100%) and stained with 100 μL of CV (0.2%) dye at room temperature for 30 min. The biofilms were then rinsed three times with PBS. Thereafter, 200 μL of ethanol (95%) was added to dissolve the dye. The remaining biofilms were quantified by measuring optical density at 590 nm with a microplate reader [49].

For the plate counting assay, the biofilms were mixed and the suspensions were diluted sequentially. The resultant 50 μL bacterial solutions were spread evenly on nutrient agar plates. After 18 h of growth in a 37°C incubator, colonies were calculated and photographed by an automatic colony enumeration instrument.

For live/dead staining, the biofilms were incubated with 100 μL stain solution (composed of 1 mL PBS, 1μLSTYO9 and 1 μL PI) and kept in the dark for 15 min. Thereafter, the biofilms were washed three times with 100 μL sterile PBS. Finally, the biofilms were observed under a CLSM [50].

Evaluation of biocompatibility *in vitro*

The cytotoxicity of IRNB was evaluated by CCK-8 and Calcein/PI cytotoxicity assays. Briefly, 3T3 cells were cultured in a clear bottom 96-well plate (5×10^3 cells per well) containing

150 μL DMEM with 10% FBS and 1% penicillin/streptomycin. The plate was incubated (37°C, 5% CO_2, 24 h) for cell attachment. The resulting medium was aspirated and replaced with a medium containing a series of IRNB concentrations (50, 100 and 500 μg/mL). A 10 μL CCK-8 solution (Solarbio, Beijing, China) was added to each well after the indicated incubation time points. Subsequently, plates were incubated for 3 h at 37°C, and the absorbance at 450 nm was measured using a microplate reader (Thermo Varioskan Flash, USA). After incubation for 48 h and 72 h, the old medium was aspirated. Then 100 μL working solution (prepared from 1 mL PBS, 1 μL PI and 1 μL CalceinAM; Beyotime, Shanghai, China) was added according to the manufacturer's instructions. After incubation for 30 min at 37°C, the cells were rinsed with PBS and observed using a CLSM. To estimate the blood compatibility of IRNB, a hemolysis activity assay was performed. First, 500 μL of mouse blood was acquired by removing the eyeballs and centrifuged at 3500 rpm for 5 min. After carefully blotting off the supernatant, the red blood cell precipitates were washed three times and resuspended in 5 mL sterile PBS. Next, a series of IRNB concentrations (50, 100 and 500 μg/mL) were mixed with 1 mL of red blood cells at 37°C for 4 h. Additionally, the DI water and PBS were included as positive and negative controls, respectively. All blood suspensions were then centrifuged at 3500 rpm for 5 min, and the absorbance of the supernatant was detected at 545 nm using a microplate reader. The hemolysis ratio was calculated using the following formula:

$$\text{Hemolysis } (\%) = (A_E - A_N) / (A_P - A_N) \times 100\%$$

where A_E, A_N and A_P represent the absorbance of the experimental well, negative control well and positive control well, respectively.

Animal models for antimicrobial treatments *in vivo*

BALB/c mice (male, 20–25 g, 6–8 weeks of age) were obtained from the Animal Experiment Center of the Army Medical University (Chongqing, China). Animal experiments were conducted following the guidelines of the Animal Experiment Ethics Committee of the Army Medical University. To evaluate the antibacterial effect of IRNB *in vivo*, we established a murine-infected full-thickness skin-defected wound model and a subcutaneous abscess model. First, mice were anesthetized by intraperitoneal injection with pentobarbital (1%, 0.01 mL/g), and the dorsal hair was shaved. The next day, the dorsal skin was sterilized with 75% (v/v) ethanol. To establish the murine-infected full-thickness skin defected wound model, two symmetrical circular wounds (diameter: 6 mm) were created on both sides of the dorsum using a biopsy punch. Next, a silicone ring (inner and outer diameters: 8 mm and 12 mm, respectively) was stitched to the margin of each wound. The two symmetrical skin wounds were then infected with an MDR *Pa* bacterial suspension (1×10^8 CFUs/mL, 50 μL). After 24 h of management, the infected wounds were successfully established. For the subcutaneous abscess model,

an MDR *Pa* bacterial suspension (1×10^8 CFUs/mL, 50 μL) was administered to the left and right back sides (subcutaneous tissue) of each test mouse, respectively. After 24 h of management, subcutaneous abscesses were successfully established on both sides of the dorsum at the injection sites.

Detection of bacteria-targeting ability of IRNB *in vivo*

After anesthetization and shaving as described above, each test mouse was subcutaneously injected with an MDR *Pa* bacterial suspension (50 μL) into the right side of the back, whereas 50 μL of sterile PBS was injected into the left side. After 24 h of management, a subcutaneous abscess was established on the right side of the back, and a sham subcutaneous abscess was established on the left side. To determine the bacteria-targeting ability of IRNB *in vivo*, the subcutaneous abscess was injected with 100 μL IRNB (100 μg/mL) in the right infected and left sham control sites. Next, live animal fluorescence imaging was applied at predefined time points (0, 6, 12, 24 and 36 h) using *ex vivo* optical imaging (AniView 100, China, excitation/emission wavelength: 730/820 nm). Furthermore, each mouse back was irradiated with an NIR laser (808 nm, 0.75 W/cm^2, 10 min) at the aforementioned time points, and an infrared camera was utilized to record the temperature. The test mice were also intravenously injected with IRNB (100 μL, 100 μg/mL) into the tail vein. Subsequently, live animal fluorescence imaging and infrared imaging were carried out as previously mentioned.

To investigate the biodistribution of IRNB, the subcutaneous abscess model mice were intravenously injected with IRNB (100 μL, 100 μg/mL) and sacrificed at the predetermined time points (days 1, 3, 7 and 28) after injection. Tissue samples, including the heart, liver, spleen, lung and subcutaneous abscess tissues were collected and photographed using a live animal fluorescence imaging system (AniView 100, China, excitation/emission wavelength: 730/820 nm).

Antimicrobial therapy *in vivo*

The mice were randomly subdivided into 10 groups (n = 3): PBS, BNN6-PEG, IR-780-PEG, IRN, IRNB, PBS + NIR, BNN6-PEG + NIR, IR-780-PEG + NIR, IRN + NIR and IRNB + NIR. For the murine-infected full-thickness skin defected wound model, each infected wound was locally inoculated with 100 μL of BNN6-PEG, IR-780-PEG, IRN and IRNB (100 μg/mL) or PBS on day 1. After 6 h inoculation, the wounds were illuminated with a laser (808 nm, 0.75 W/cm^2, 10 min) or kept in the dark according to the groups described above. The infected wounds were observed and photographed at the indicated time points. Wound area was estimated by Image J software. The following formula was used to calculate the wound healing rate:

$$\text{Wound healing rate } (\%) = (W0 - WR) / W0 \times 100\%$$

where W0 indicates the wound area on day 0, and WR indicates the residual wound area on days 1, 3, 5, 7, and 9, respectively.

Nine days later, wound tissues were cut and homogenized for bacterial burden counting and harvested for histological analysis (Hematoxylin and eosin [H&E] staining, Masson staining, and IL-6, TNF-α and CD31 immunofluorescence staining).

For the subcutaneous abscess model, 100 μL BNN6-PEG, IR-780-PEG, IRN and IRNB dispersions (100 μg/mL), IRNB dispersion (200 μg/mL), or PBS was injected into the subcutaneous abscess, respectively. Six hours post-injection, the subcutaneous abscess site was irradiated with a laser (808 nm, 0.75 W/cm², 10 min). After 10 days of treatment, the subcutaneous abscesses were biopsied and photographed. Similarly, the abscess tissues were collected for bacterial colony counting and H&E staining. All the above slides were scanned using a slide scanner (SLIDEVIEW VS200, Olympus).

Toxicity evaluation of IRNB *in vivo*
BALB/c mice (n = 3) were utilized to evaluate the toxicity of IRNB *in vivo*. After injection of 100 μL sterile PBS or IRNB dispersions (50, 100 and 500 μg/mL) into the tail vein, the mice were sacrificed on day 9. Tissue samples, including the heart, liver, spleen, lung and kidney were collected for H&E staining. Histological slides were scanned using a slide scanner. In addition, blood specimens were collected for blood and biochemistry analysis on day 9.

Statistical analysis
The data were presented as mean ± standard deviation, and the statistically significant difference between the groups was analyzed using one-way or two-way analysis of variance with SPSS statistics 22.0. Tukey's *post hoc* test or Dunnett's T3 *post hoc* test were used for multiple comparisons. The statistical significance was set as follows: $^*P < 0.05$, $^{**}P < 0.01$, and $^{***}P < 0.001$.

Results

Synthesis and characterization of IRNB
The IR-780 and BNN6 molecules are hydrophobic; therefore, the IRNB NPs could be synthesized according to the solvent exchange method described previously [51]. Briefly, IR-780 iodide and BNN6 were dispersed in CH_3CN to form a stock solution. Lecithin and DSPE-PEG-PBA were then dissolved in DI water and vigorously stirred (60°C, 30 min). Next, the IR-780 iodide/BNN6/CH_3CN solution was dripped into a preheated solution, followed by magnetic stirring for another 2 h. The original IRNB NP suspensions were centrifuged (3000 rpm, 10 min) and dialyzed using an 8 kDa MWCO dialysis bag for 4 h in DI water to remove free CH_3CN, IR-780, BNN6, lecithin and DSPE-PEG-PBA. At this point the IRNB NPs had been successfully synthesized. Other NP counterparts (IR-780-PEG, BNN6-PEG and IRN NPs) were also prepared based on the above method. As shown in Figure 2a, the FTIR spectrum of IRNB presented a C-Cl stretch at 720 cm^{-1}, CN stretch at 1176 cm^{-1} and C=C

stretch at 1550 cm^{-1}, indicating the character of IR-780. In addition, a peak at 1377 cm^{-1} indicated the deformation of N-N=O, manifesting the successful loading of BNN6. The peak at 1450 cm^{-1} indicated C-B vibration, verifying the presence of PBA. The morphological features, size distributions and optical features of IRNB were characterized by TEM, DLS and UV–Vis spectra, respectively. TEM characterization revealed that IRNB NPs were monodispersed and spherical in morphology with diameters ranging from 200–250 nm (Figure 2b). In addition, the hydrodynamic sizes of IRNB (peak: 220.194 nm), IRN (peak: 190.137 nm), IR-780-PEG (peak: 164.183 nm) and BNN6-PEG (peak: 220.194 nm), suggested that they were well-dispersed and had similar sizes in water (Figure 2c). In addition, we also found that IRNB was negatively charged (-14.83 ± 1.35 mV) according to its zeta potential (Figure 2d). Furthermore, the hydrodynamic stability of IRNB was evaluated by measuring the hydrodynamic diameter under different conditions. As shown in Supplementary Figure S1a, the hydrodynamic diameter changed from 217.1 ± 2.51 nm to 247.6 ± 8.68 nm, 222.07 ± 3.07 nm to 270.53 ± 8.33 nm, and 212.3 ± 1.97 nm to 227.2 ± 4.26 nm in DI water, PBS and PBS containing 10% FBS at 4°C within 7 days, respectively.

Release profiles of IRNB
To study the activity of IRNB under NIR laser or kept in the dark, the *in vitro* release test was carried out. As shown in Supplementary Figure S1b, c, the standard curves of IR-780 and BNN6 were drawn by a UV–Vis spectrophotometer. Then the concentrations were determined based on the standard curve. As shown in Supplementary Figure S1d, e, IR-780 and BNN6 were slowly released from IRNB and reached $19.41 \pm 4.31\%$ and $16.19 \pm 3.59\%$ at day 7 when protected from light. In contrast, IR-780 and BNN6 were quickly released from IRNB and reached $82.11 \pm 6.6\%$ and $69.81 \pm 5.77\%$ within 12 h after NIR laser irradiation.

Optical and photothermal properties of IRNB
As a typical heptamethine cyanine dye, IR-780, demonstrated near-infrared absorption, a fluorescent nature and a photothermal effect, showing promising prospects for use in treating preclinical cancer and infectious models [52,53]. Furthermore, an 808 nm NIR laser is widely applied in IR-780 mediated therapies owing to its excellent absorption property in the NIR spectrum [54,55]. As a result, the optical absorption of free BNN6, free IR-780, BNN6-PEG, IR-780-PEG, IRN and IRNB were analyzed using a UV–Vis–NIR spectrometer. As shown in Figure 2e, free BNN6, free IR-780, BNN6-PEG, IR-780-PEG, IRN and IRNB exhibited absorbances of 0.048, 0.12, -0.038, 0.503, 0.517 and 0.756 at 808 nm, respectively. As shown in Supplementary Figure S1f, the normalized fluorescent spectra of IRNB confirmed its fluorescence nature. In order to investigate the PTT efficiency of IRNB, temperature changes (0–250 μg/mL) under laser illumination (808 nm, 0.5–1.0 W/cm², 11 min) were recorded.
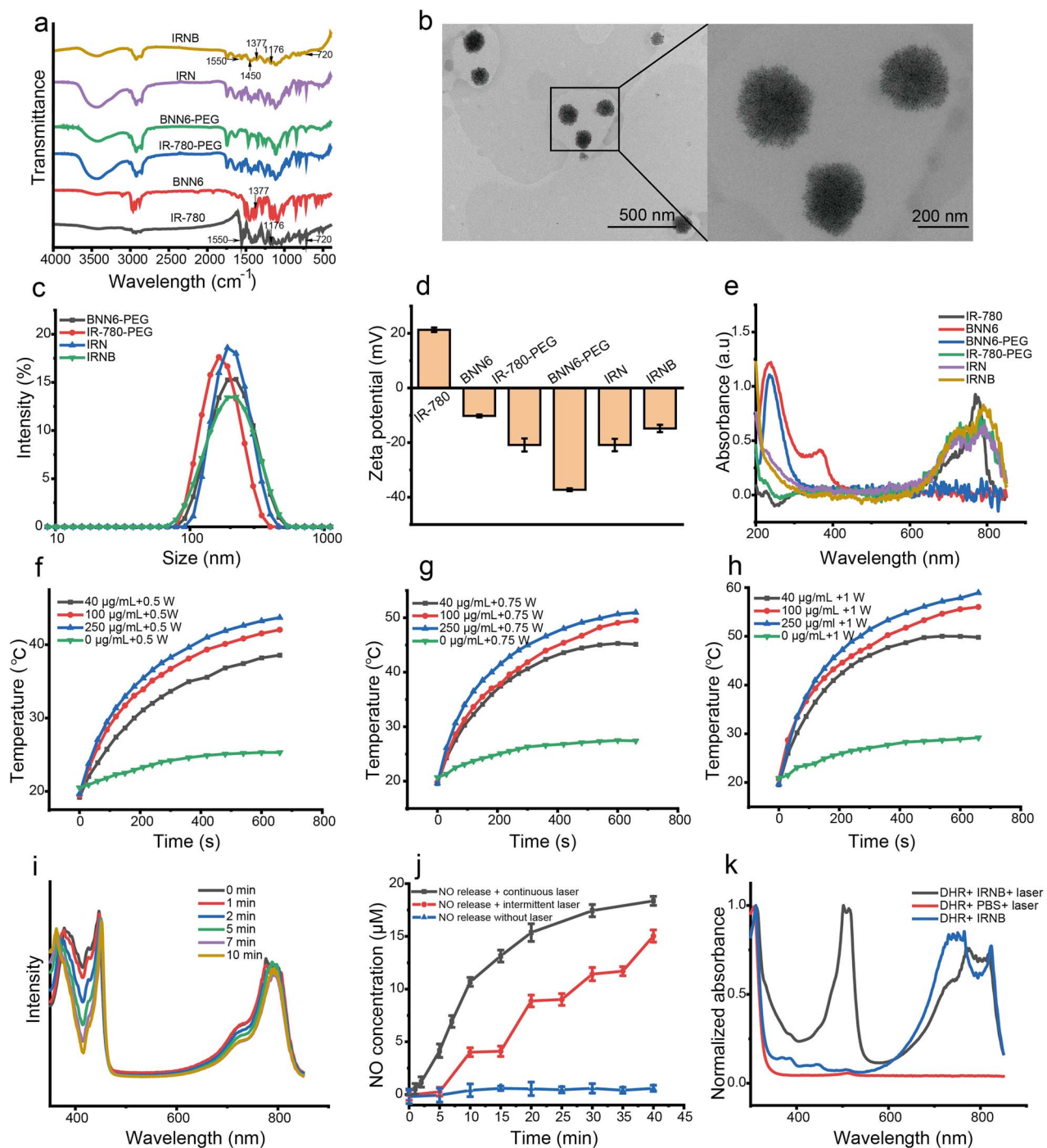
Figure 2. Characterization of IRNB. (**a**) FTIR spectra of free IR-780, free BNN6, synthesized IR-780-PEG, BNN6-PEG, IRN and IRNB. (**b**) TEM images of IRNB nanoparticles (Scale bar: 500 nm and 200 nm). (**c**) and (**d**) Hydrodynamic diameter and ζ potential of IR-780-PEG, BNN6-PEG, IRN and IRNB in PBS buffer measured by DLS. (**e**) UV–Vis absorption spectra of free IR-780, free BNN6, synthesized IR-780-PEG, BNN6-PEG, IRN and IRNB. (**f**), (**g**) and (**h**) Temperature evolution curves of IRNB with different concentrations (0–250 μg/mL) under 808 nm NIR irradiation at 0.5, 0.75 and 1 W/cm^2. (**i**) UV–Vis absorbance spectrum of IRNB co-incubated with DPBF under 808 nm NIR irradiation at 0.75 W/cm^2 for different time periods. (**j**) NO release profile of IRNB under different laser irradiation conditions. (**k**) DHR 123 UV–Vis absorbance spectrum after various treatments. *FTIR* fourier transform infrared spectroscopy, *BNN6* N,N′-di-sec-butyl-N,N′-dinitroso-1,4-phenylenediamine, *IRN* IR-780/BNN6-PEG, *IRNB* IR-780/BNN6-PEG-PBA, *TEM* transmission electron microscopy, *PBS* phosphate-buffered saline, *DLS* dynamic light scattering, *NIR* near infrared laser, *DPBF* 1,3-diphenylisobenzofuran, *NO* nitric oxide, *DHR* 123 dihydrorhodamine 123, *UV–Vis* ultraviolet–visible

As shown in Figure 2f, g and h, PBS was a blank control and we observed a slight temperature change from 20.5°C to 25.3°C (0.5 W/cm^2), 20.7°C to 27.4°C (0.75 W/cm^2), 20.9°C

to 29.2°C (1 W/cm^2) after 10 min. Under the power density of 0.5 W/cm^2, 0.75 W/cm^2 and 1.0 W/cm^2 for 10 min, the temperatures of the 100 μg/mL IRNB increased from 19.45°C to

42.03°C, 19.8°C to 49.5°C, and 20.7°C to 56.03°C, demonstrating a concentration- and time-dependent temperature enhancing pattern. Besides, the η was measured based on the previously reported method [56]. As shown in Supplementary Figure S1g, h, IRNB exhibited η value of 26.75%, making it a promising PTT agent. Furthermore, as shown in Supplementary Figure S1i, good photostability of IRNB was observed after 5 cycles of ON/OFF laser irradiation. To avoid surrounding tissues receiving undesirable burns resulting from high temperature (>55°C), 100 μg/mL IRNB with 0.75 W/cm² laser was selected for antibacterial treatment for subsequent experiments.

Photodynamic effect of IRNB
IR-780 can generate $^1O_2$ upon irradiation with an NIR laser [57]. The depletion of DPBF was utilized to illustrate the $^1O_2$ generation based on the previously reported method [15,58]. Typically, the characteristic absorption at 410 nm of DPBF can decrease with the presence of $^1O_2$. As shown in Figure 2i and Supplementary Figure S1j, after the incubation of DPBF and IRNB, the absorbance intensity at 410 nm decreased by 68.335% following NIR laser illumination, suggesting an excellent photodynamic effect.

Controllable NO release of IRNB
A Griess kit was utilized to investigate the production of NO, which would convert into NO^{2-} in an aqueous solution. NO^{2-} reacted with the Griess reagent and the concentrations were calculated based on a standard curve. As shown in Figure 2j, for IRNB without laser irradiation, there was approximately 0.59 ± 0.29 μM production of NO gas after 40 min. However, IRNB revealed a total 18.37 ± 0.45 μM NO gas production after being irradiated with a continuous NIR laser. These results revealed that laser irradiation of IRNB prompted the release of NO gas in a photothermal-dependent manner, as previously reported [15,59]. In addition, NO release under intermittent laser irradiation was observed. When the laser was turned on for 5 min, IRNB released 4.01 ± 0.42 μM NO gas. Nevertheless, IRNB released 0.14 ± 0.49 μM NO gas when the laser was turned off for another 5 min.

RNS generation and detection
RNS has been reported to generate free radical peroxidation and is regarded as a more lethal oxidant [40]. In an aqueous solution, reactions between NO and ROS could produce peroxynitrite anions $ONOO^-$, which belongs to one of the major types of RNS [40]. Furthermore, DHR can be exclusively oxidized by $ONOO^-$ and produce rhodamine 123, which induced characteristic absorption at 505 nm [42,60]. As shown in Figure 2k, a significant absorption peak at 505 nm was measured in the IRNB group following NIR laser irradiation, suggesting that $ONOO^-$ was produced. Conversely, almost no $ONOO^-$ was observed in the IRNB

without laser group and PBS with laser group, considering the relatively low absorbance at 505 nm. These results showed that $ONOO^-$ could also be generated in the presence of NO and ROS in the IRNB group following NIR laser irradiation. Furthermore, the generation of $ONOO^-$ might greatly enhance the bactericidal effects of IRNB [15,42].

In vitro bacteria-targeting abilities of IRNB
Large amounts of lipopolysaccharide (LPS) are the main structural cell wall component of gram-negative bacteria. These can be effectively bound by PBA to form cyclic boronic esters via the formation of a pair of covalent bonds [60–62]. Accordingly, we speculated that IRNB could selectively bind to gram-negative bacterial cells. Clinically isolated *Ab*, *Kp* and *Pa* strains were selected as representative gram-negative bacteria. After incubation with BNN6-PEG, IR-780-PEG, IRN and IRNB for 30 min at 37°C, followed by centrifugation and rinsing, the free nanomaterials were removed. Following laser irradiation (808 nm, 0.75 W/cm², 10 min), the interactions between bacteria and IRNB were investigated via thermographic imaging. As shown in Figure 3a, b, the temperatures of the IRNB-treated groups were 48.6 ± 1.45°C (*Ab*), 48.93 ± 0.55°C (*Kp*) and 48.23 ± 1.00°C (*Pa*), respectively. However, the temperatures in the control groups remained between $25 \sim 33$°C. The increased temperatures of the IRNB-treated groups were primarily due to their high affinities toward gram-negative bacteria. Additionally, SEM was employed to visually investigate the binding capability of IRNB toward bacteria. As shown in Figure 3c, almost all bacteria were closely surrounded by IRNB. In contrast, no other nanoparticles were found near bacteria in the control groups. These results showed that IRNB could specifically target gram-negative bacteria.

NIR-triggered ROS/NO generation in bacterial cells
In addition to the measurements of ROS and NO production in the extracellular environment reported above, we also measured ROS and NO production in the MDR *Ab*, *Kp* and *Pa* bacterial cells via *in situ* imaging. DCFH-DA can be cleaved intracellularly and subsequently react with ROS to produce bright green fluorescent 2′,7′-dichlorodihydrofluorescein [63], which was utilized to detect ROS. As shown in Figure 4a, c and Supplementary Figure S2, strong green DCFH-DA fluorescence was observed in IRNB-treated MDR *Ab*, *Kp* and *Pa* groups following irradiation with an NIR laser, suggesting that the IRNB group shows NIR laser-responsive ROS generation. Furthermore, as shown in Supplementary Figure S3, the fluorescence spectra quantitatively measured intracellular ROS. Upon NIR laser irradiation, the IRNB group presented more ROS generation in bacteria, which was consistent with the laser confocal imaging results. Moreover, the relative ROS levels of IR-780-PEG and IRN-treated MDR *Ab*, *Kp* and *Pa* groups were $40\% \pm 5.04\%$, $41.36\% \pm 1.17\%$, $43.69\% \pm 4.72\%$,
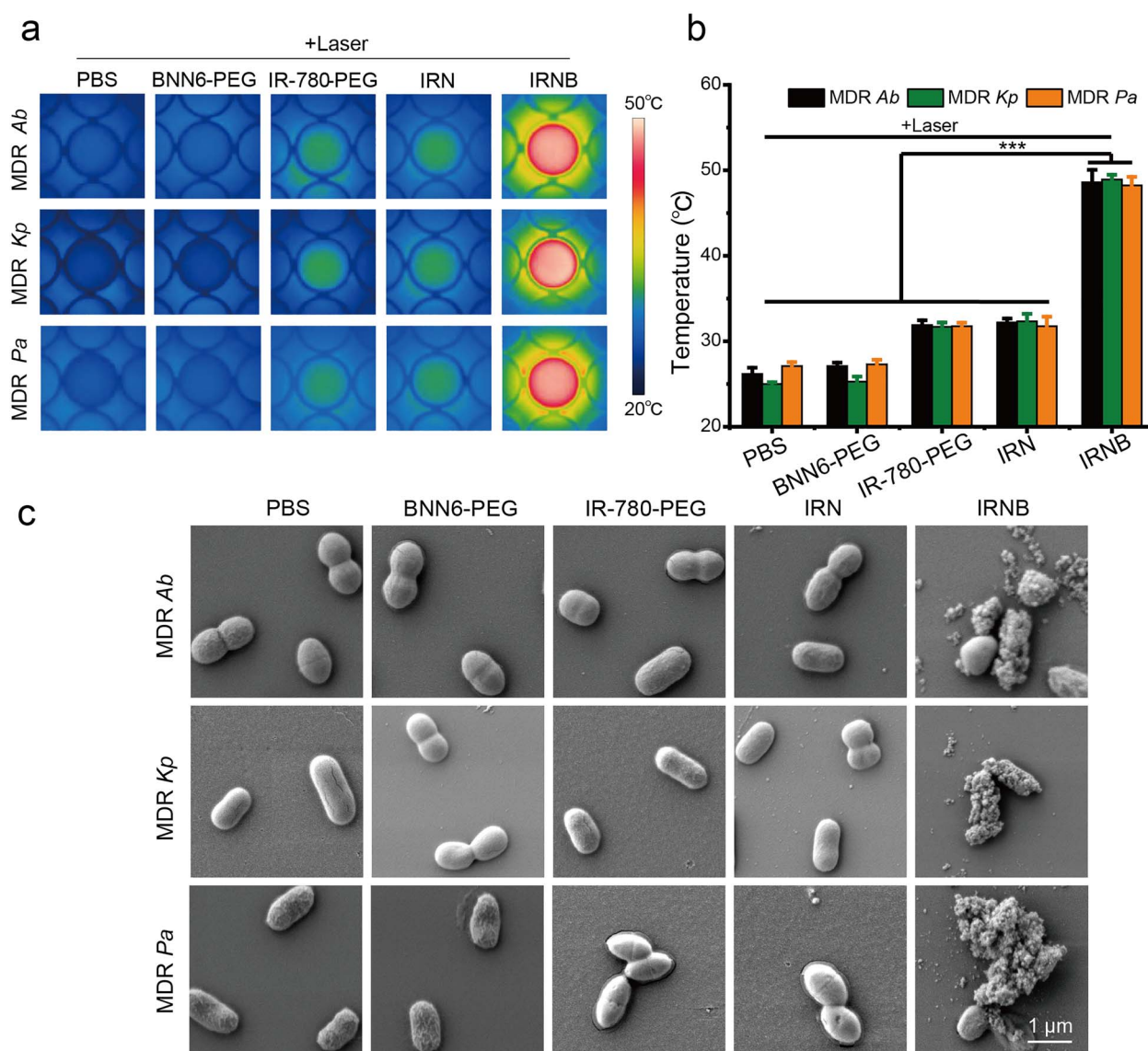
Figure 3. *In vitro* bacteria-targeting abilities of IRNB. (**a**) and (**b**) Thermographic images and the corresponding temperature measurements of MDR *Ab*, MDR *Kp* and MDR *Pa* suspensions after incubation with PBS, IR-780-PEG, BNN6-PEG, IRN and IRNB under laser irradiation (808 nm, 0.75 W/cm^2,10 min). Statistical analysis: Mean ± SD; n = 3; ∗∗∗$p < 0.001$, ∗∗$p < 0.01$, ∗$p < 0.05$. (**c**) Representative SEM images of MDR *Ab*, MDR *Kp* and MDR *Pa* after incubation with PBS, IR-780-PEG, BNN6-PEG, IRN and IRNB (Scale bar: 1 μm). *BNN6* N,N′-di-sec-butyl-N,N′- dinitroso-1,4-phenylenediamine, *IRN* IR-780/BNN6-PEG, *IRNB* IR- 780/BNN6-PEG-PBA, *MDR* multidrug-resistant, *Ab Acinetobacter baumannii*, *Kp Klebsiella pneumoniae*, *Pa Pseudomonas aeruginosa*, *SEM* scanning electron microscopy, *PBS* phosphate-buffered saline

42.68% ± 5.36%, 44.06% ± 1.90% and 50.79% ± 3.65%, respectively. This might be because of the nonspecific binding between IR-780-PEG, IRN and bacterial cells.

The commercial NO fluorescence probe DAF-FM DA can be cleaved intracellularly and react with NO^{2-} to generate a green fluorescent DAF-FM triazole derivative. Here, DAF-FM DA was utilized to detect intracellular NO levels [64,65]. As shown in Figure 4b, d and Supplementary Figure S4, a strong green fluorescence was observed in IRNB-treated MDR *Ab*, *Kp* and *Pa* + NIR laser groups, demonstrating that IRNB is associated with NIR-responsive NO generation. In addition, IRN-treated MDR *Ab*, *Kp* and *Pa* groups presented

relative NO levels of 46.40% ± 5.63%, 44.82% ± 4.52% and 41.28% ± 5.61%, respectively, which was also probably caused by nonspecific binding between IRN and bacterial cells.

In vitro antibacterial and antibiofilm activities of IRNB
The above *in vitro* experiments reveal that IRNB generated hyperthermia, ROS and NO following 808 nm laser illumination. Thus, the antibacterial and antibiofilm properties of IRNB were first investigated *in vitro*. As shown in Figure 5, the plate counting method was used to quantitatively measure the antibacterial efficiency of IRNB
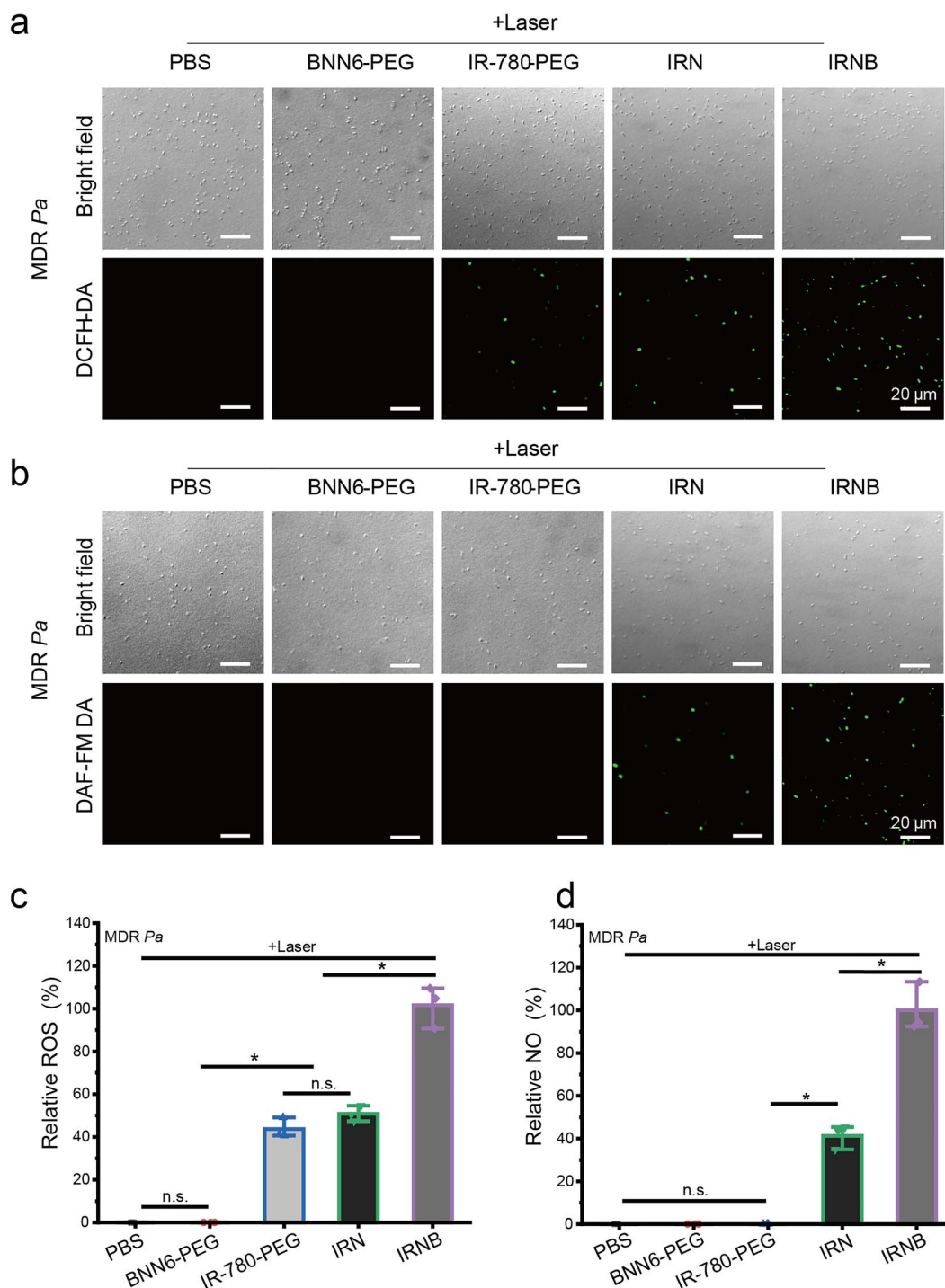
Figure 4. NIR-triggered ROS/NO generation in bacterial cells. (**a**) and (**c**) Confocal laser microscopy images and relative quantitative fluorescence intensity bar chart of ROS generation in MDR *Pa* after receiving various treatments (Scale bar: 20 μm). (**b**) and (**d**) Confocal laser microscopy images and relative quantitative fluorescence intensity bar chart of NO generation in MDR *Pa* after receiving various treatments (Scale bar: 20 μm). Statistical analysis: Mean $\pm$ SD; n = 3; $***p < 0.001$, $**p < 0.01$, $*p < 0.05$. *NIR* near infrared laser, *ROS* reactive oxygen species, *NO* nitric oxide, *MDR* multidrug-resistant, *Pa Pseudomonas aeruginosa*, *PBS* phosphate-buffered saline, *BNN6* N,N′-di-sec-butyl-N,N′- dinitroso-1,4-phenylenediamine, *IRN* IR-780/BNN6-PEG, *IRNB* IR-780/BNN6-PEG-PBA, *DCFH-DA* 2′,7′-Dichlorodihydrofluorescein diacetate, *DAF-FM DA* 4-Amino-5-methylamino-2′,7′-difluorofluorescein diacetate

and its control counterparts (PBS, BNN6-PEG, IR-780-PEG and IRN) against gram-negative MDR *Ab*, *Kp* and *Pa* with or without NIR laser irradiation. In the absence of an NIR laser, none of the groups showed an obvious antibacterial effect.

However, upon NIR laser illumination (808 nm, 0.75 W/cm^2, 10 min), the bacterial viabilities of the IRNB-treated groups were 0.52% $\pm$ 0.19%, 1.74% $\pm$ 0.62% and 2.96% $\pm$ 0.45% for MDR *Ab*, *Kp* and *Pa*, respectively. These results revealed

that more than 95% of planktonic MDR *Ab*, *Kp* and *Pa* were eradicated by the IRNB + laser, which indicated a potent bactericidal activity via the synergism of PTT, PDT and NO. In addition, the PBS + laser and BNN6-PEG + laser-treated groups also presented no obvious antibacterial effect. The bacterial viability of the IR-780-PEG + laser-treated MDR *Ab*, *Kp* and *Pa* groups was 53.97% ± 1.54%, 58.96% ± 3.62% and 57.71% ± 2.51%, respectively. The photothermal temperatures were 31°C ∼ 33°C for the IR-780-PEG + laser-treated groups as described in Figure 3a, b, which were too low to generate a bactericidal effect. In addition, Figure 4a, c also revealed the presence of intracellular ROS in some bacteria. Therefore, the bactericidal efficacy of the IR-780-PEG + laser could be attributed to the nonspecific binding between IR-780-PEG and the bacteria as well as the NIR-responsive bactericidal effect of PDT. Meanwhile, the bacterial viability of the IRN + laser-treated MDR *Ab*, *Kp* and *Pa* groups was 30.32% ± 1.10%, 39.95% ± 4.33% and 29.51% ± 2.39%, respectively. Similarly, the IRN + laser-treated groups revealed a photothermal temperature of 31°C ∼ 34°C, and showed intracellular ROS and NO in some bacteria, as indicated in Figure 4b, d. Hence, the bactericidal effect of the IRN + laser could also be attributed to the nonspecific binding capability of IRN toward bacteria and the NIR-responsive bactericidal effect of PDT and NO [15]. These results manifested that BNN6-PEG, IR-780-PEG, IRN and IRNB with NIR laser irradiation showed an increasing trend in bactericidal efficacy. Particularly, IRNB + laser treatment displayed the highest bactericidal efficiency toward MDR gram-negative bacteria by virtue of its bacteria-specific targeting ability and the synergistic effects of PTT, PDT and NO gas therapy.

To further investigate the synergistic antibacterial effect of IRNB, a live/dead staining was conducted. SYTO9 can enter all bacterial cells and stain bacteria with green fluorescence, whereas PI is only allowed to enter into bacterial cells via impaired cell membranes and stain dead bacteria with red fluorescence [66]. As shown in Figure 6a, the PBS/BNN6-PEG + laser-treated groups presented only bacteria that were stained with green fluorescence. At the same time, a gradually increasing trend was observed in the red fluorescence intensities of the bacteria treated with IR-780-PEG + laser, IRN + laser and IRNB + laser. The corresponding quantitative analysis was carried out based on the ratios of red/green fluorescent bacteria. As presented in Figure 6b–d, the IR-780-PEG + laser-treated groups showed bacterial viabilities of 47.73% ± 3.78%, 52.91% ± 2.44% and 52.99% ± 4.21% for the MDR *Ab*, *Kp* and *Pa* (*P* < 0.01) groups, respectively. Furthermore, the IRN + laser-treated groups showed bacterial viabilities of 26.08% ± 2.40%, 34.15% ± 3.13% and 34.17% ± 3.28% for the MDR *Ab*, *Kp* and *Pa* (*P* < 0.001) groups, respectively. Finally, the bacteria that received the IRNB + laser treatment exhibited the lowest viabilities (1.67% ± 2.58%, 1.38% ± 1.23% and 1.75% ± 0.39% for MDR *Ab*, *Kp* and *Pa*, respectively; *P* < 0.001). Overall, all the live/dead staining results

were consistent with the plate counting results reported above.

To observe the interaction between IRNB and the MDR *Ab*, *Kp* and *Pa* cells directly, TEM was used. As shown in Figure 6e, intact bacterial cell walls and uniformly distributed cytoplasm were presented in bacterial cells from the PBS/BNN6-PEG + laser-treated groups. Meanwhile, we observed some incomplete bacterial cell walls and cytoplasm leakage in the IR-780-PEG/IRN + laser-treated groups. However, for the IRNB + laser-treated group, the bacterial cell walls were severely distorted and cracked. Several bubbles emerged in the cytoplasm, with some cytoplasm distributed loosely outside the cell walls, indicating permanent destruction of the interior structures.

After demonstrating the bactericidal effect of IRNB against planktonic bacteria, the antibacterial properties against refractory bacterial biofilms were analyzed by crystal violet (CV) staining assay, plate counting method and live/dead staining. As shown in Supplementary Figure S5, the CV staining results suggested that IRNB could eliminate biofilms efficiently with NIR laser illumination. As shown in Figure 7a–c, all the groups without laser irradiation or the PBS/BNN6-PEG + laser groups showed no obvious antibiofilm effects. However, the bacterial viabilities of the IR-780-PEG + laser-treated MDR *Ab*, *Kp* and *Pa* biofilm groups were 76.09% ± 7.53%, 62.89% ± 3.30% and 74.24% ± 6.31%, respectively. The bacterial viabilities of the IRN + laser-treated MDR *Ab*, *Kp* and *Pa* biofilm groups were 58.00% ± 3.68%, 42.75% ± 5.44% and 58.18% ± 5.99%, respectively. In contrast, following NIR laser application (0.75 W/cm², 10 min), IRNB could eradicate ∼70% and ∼95% of biofilms at concentrations of 100 and 200 μg/mL, respectively (the bacterial viabilities were 27.48% ± 1.82% and 1.72% ± 0.60% for MDR *Ab* biofilms, 25.31% ± 2.30% and 2.00% ± 0.69% for MDR *Kp* biofilms, and 32.27% ± 2.20% and 2.78% ± 0.45% for MDR *Pa* biofilms, respectively). These results indicated that IRNB + laser treatment could effectively eradicate MDR gram-negative biofilms, and that the biofilm ablation efficacy of IRNB was enhanced in a concentration-dependent manner. Furthermore, bacterial viabilities within the biofilms were investigated by live/dead staining, and biofilm images were assessed via 3D CLSM. As shown in Figure 7d, after NIR laser irradiation, the IRNB group presented far more red fluorescent spots compared to its counterparts (PBS, BNN6-PEG, IR-780-PEG and IRN), and showed a concentration-dependent bactericidal behavior. These results strongly demonstrated that IRNB has great potential as an antimicrobial candidate against MDR gram-negative bacteria and their biofilms.

In vivo biodistribution of IRNB

Previous studies have suggested that IR-780 can be utilized as an excellent agent for fluorescence imaging *in vivo* [28,52]. The fluorescent nature of IRNB was also confirmed in our present study (Supplementary Figure S1f). To explore whether
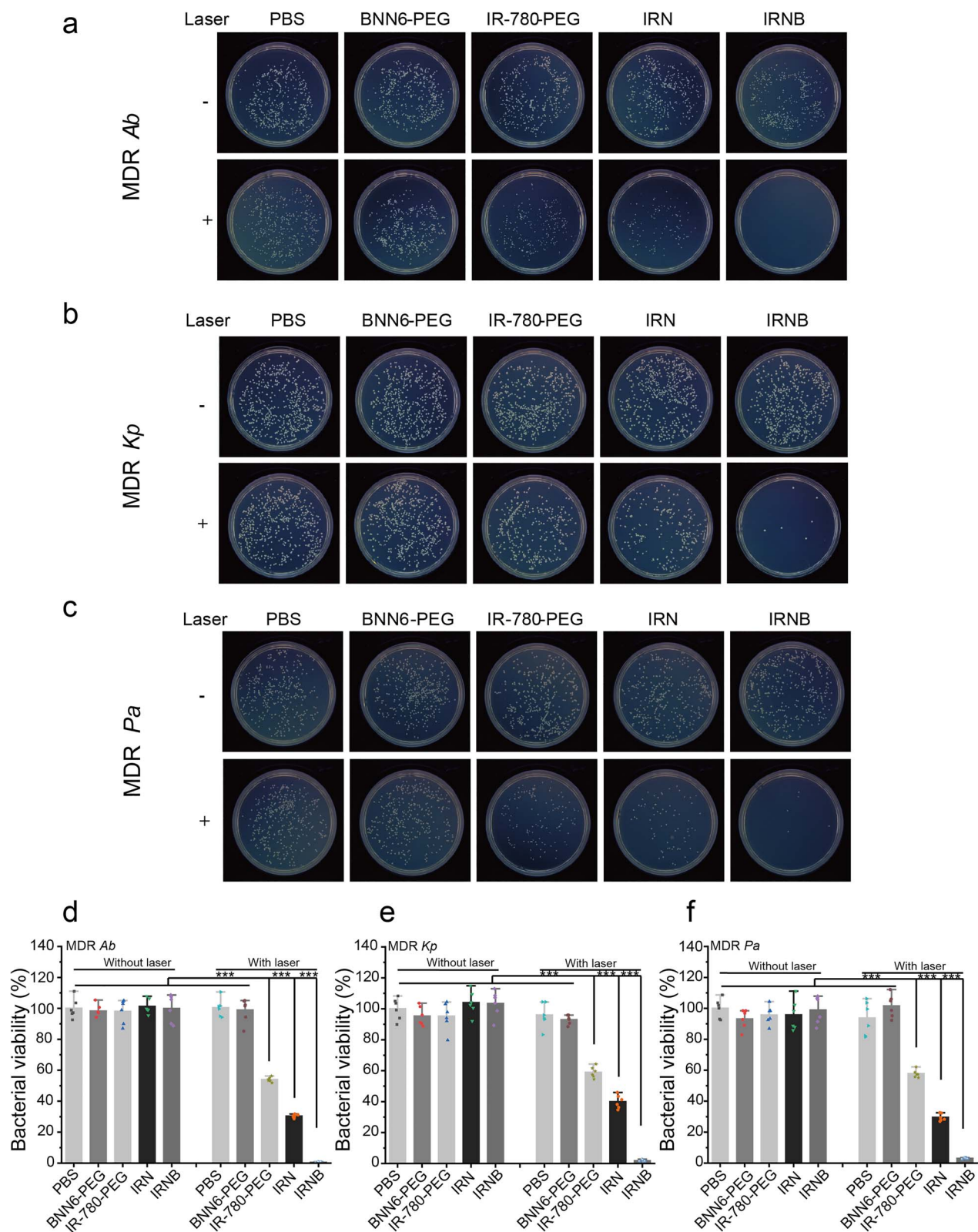
Figure 5. *In vitro* antibacterial activities of IRNB. (**a**), (**b**) and (**c**) Representative images of bacterial CFUs of MDR *Ab*, MDR *Kp* and MDR *Pa* exposed to PBS, IR-780-PEG, BNN6-PEG, IRN and IRNB with or without laser irradiation. (**d**), (**e**) and (**f**) Relative bacterial viability analysis of MDR *Ab*, MDR *Kp* and MDR *Pa* after receiving different treatments. Statistical analysis: Mean $\pm$ SD; n = 6; ∗∗∗$p < 0.001$, ∗∗$p < 0.01$, ∗$p < 0.05$. *MDR* multidrug-resistant, *CFU* colony forming unit, *PBS* phosphate-buffered saline, *BNN6* N,N′-di-sec-butyl- N,N′- dinitroso-1,4-phenylenediamine, *IRN* IR-780/BNN6-PEG, *IRNB* IR-780/BNN6-PEG-PBA, *Ab Acinetobacter baumannii*, *Kp Klebsiella pneumoniae*, *Pa Pseudomonas aeruginosa*
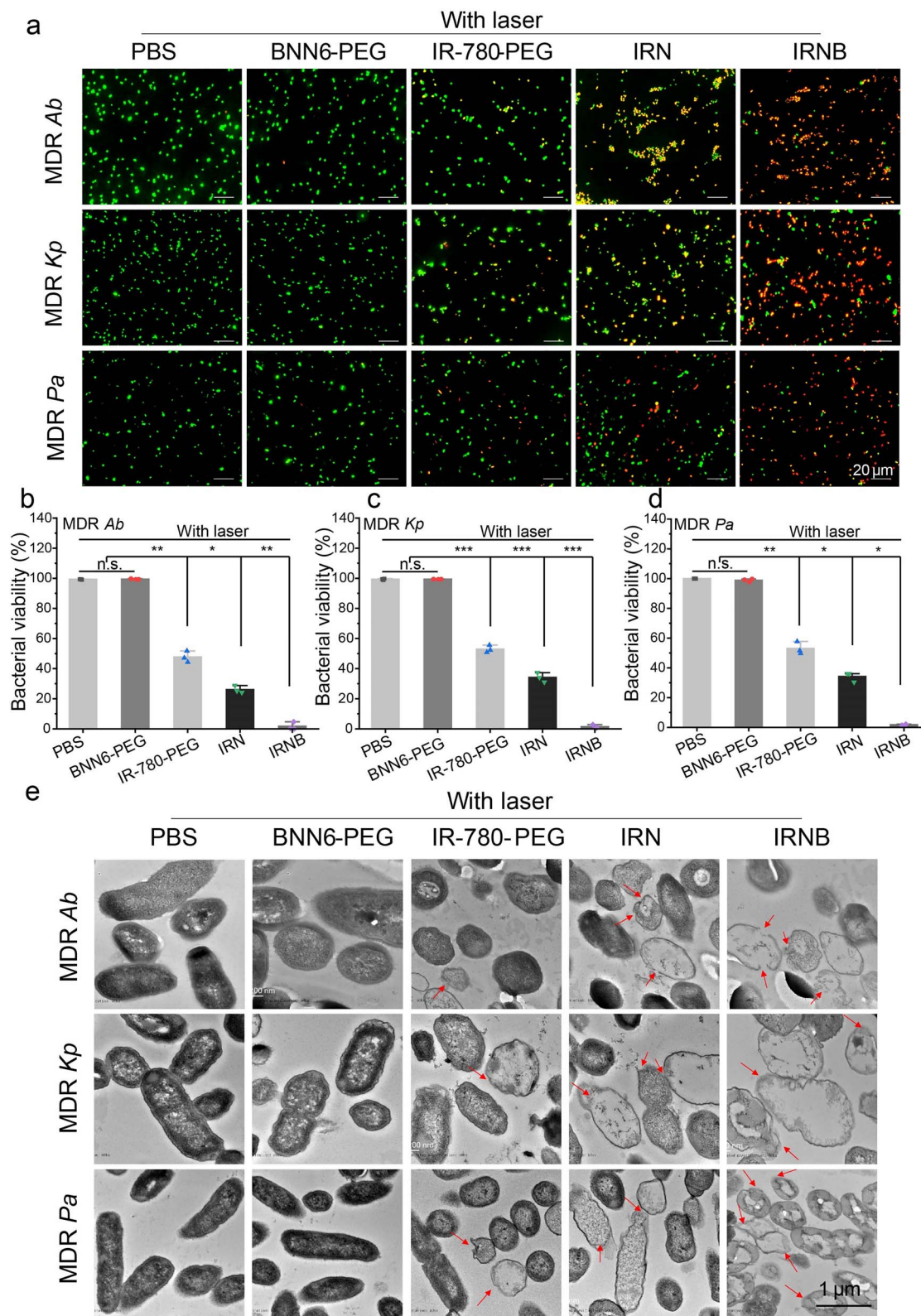
Figure 6. *In vitro* antibacterial mechanisms of IRNB. (**a**) Live/dead staining of MDR *Ab*, MDR *Kp* and MDR *Pa* exposed to PBS, IR-780-PEG, BNN6-PEG, IRN and IRNB with laser irradiation (Scale bar: 20 μm). (**b**), (**c**) and (**d**) Relative bacterial viability analysis of MDR *Ab*, MDR *Kp* and MDR *Pa* after receiving different treatments. Statistical analysis: Mean $\pm$ SD; n = 3; $***p < 0.001$, $**p < 0.01$, $*p < 0.05$. (**e**) Representative TEM images of MDR *Ab*, MDR *Kp* and MDR *Pa* after receiving different treatments (Scale bar: 1 μm). The arrows indicated the disrupted bacterial membranes. *IRNB* IR-780/BNN6-PEG-PBA, *MDR* multidrug-resistant, *PBS* phosphate-buffered saline, *BNN6* N,N'-di-sec-butyl-N,N'- dinitroso-1,4-phenylenediamine, *IRN* IR- 780/BNN6-PEG, *Ab Acinetobacter baumannii*, *Kp Klebsiella pneumoniae*, *Pa Pseudomonas aeruginosa*, *TEM* transmission electron microscopy
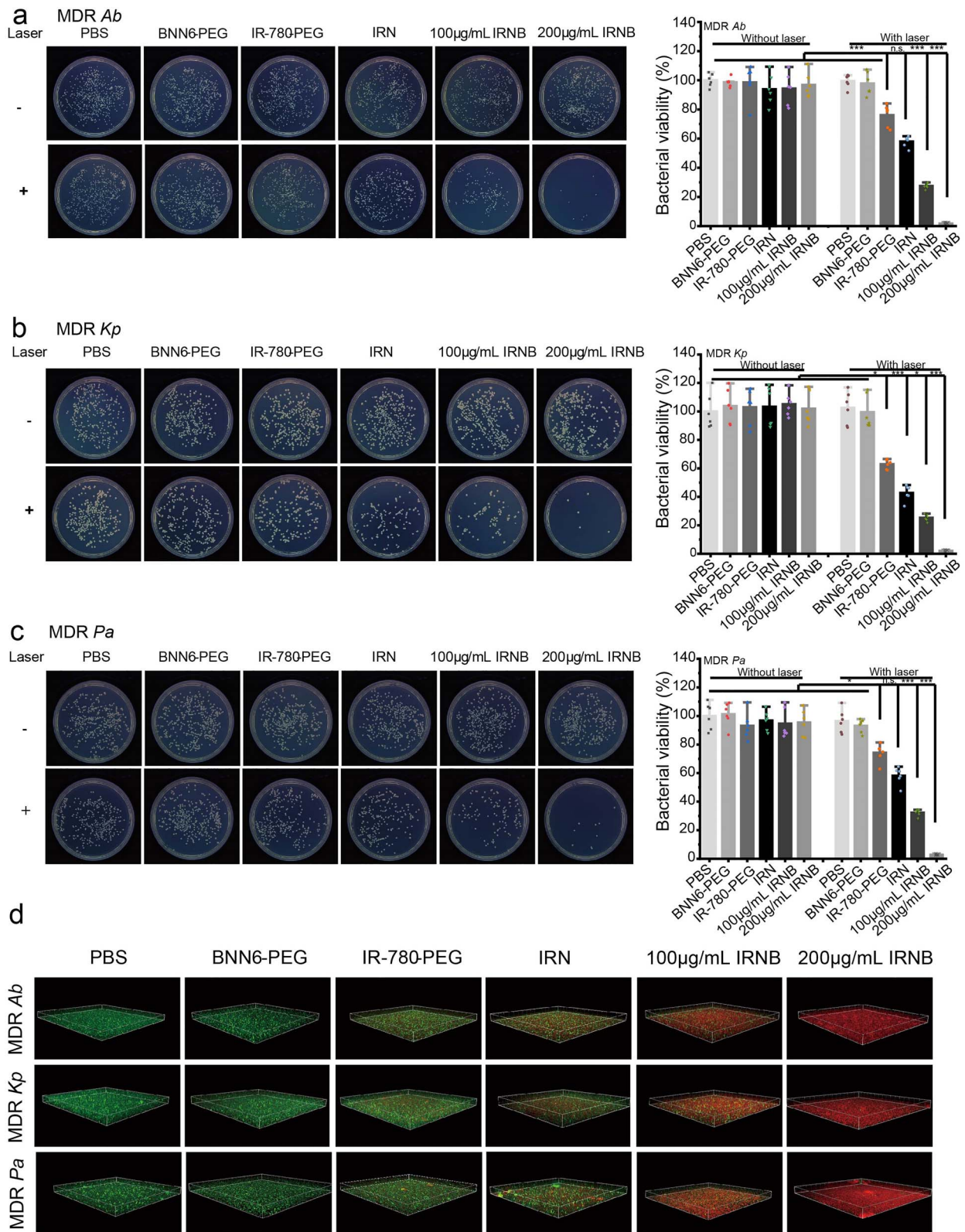
Figure 7. *In vitro* antibiofilm activities of IRNB. **(a–c)** Representative images and their relative bacterial viability analysis of bacterial CFUs of MDR *Ab*, MDR *Kp* and MDR *Pa* biofilm exposed to PBS, IR-780-PEG, BNN6-PEG, IRN, 100 μg/mL IRNB and 200 μg/mL IRNB with or without laser irradiation. Statistical analysis: Mean ± SD; n = 6; ∗∗∗$p < 0.001$, ∗∗$p < 0.01$, ∗$p < 0.05$. **(d)** Live/dead staining of MDR *Ab*, MDR *Kp* and MDR *Pa* biofilms after receiving different treatments. *IRNB* IR-780/BNN6-PEG-PBA, *CFU* colony forming unit, *MDR* multidrug-resistant, *PBS* phosphate-buffered saline, *BNN6* N,N′-di-sec-butyl-N,N′- dinitroso-1,4-phenylenediamine, *IRN* IR-780/BNN6-PEG, *Ab Acinetobacter baumannii*, *Kp Klebsiella pneumoniae*, *Pa Pseudomonas aeruginosa*

IRNB could gather at the site of bacterial infection, both *in vivo* fluorescence imaging and thermal imaging were implemented. As shown in Figure 8a–c, the right side contained subcutaneous abscesses and the left flank was a sham abscess on the dorsum of the mouse. Following intravenous injection with IRNB, the fluorescence signal intensity of the subcutaneous abscess elevated progressively, reaching a peak 24 h after injection. Nevertheless, no fluorescence signal was measured in the sham abscess. Consistent with the *in vivo* fluorescent imaging, the thermal images revealed that the temperature in the subcutaneous abscess had also shown a gradual increase with time, and reached a peak 24 h after injection. In contrast, the temperature in the sham abscess was unchanged.

As shown in Figure 8d–f, after local inoculation with IRNB, the fluorescence signal intensity and hyperthermia of the subcutaneous abscess increased progressively and peaked at 6 h post-injection, whereas decreasing fluorescence intensity and temperature were observed in the sham abscess. Moreover, to observe the biodistribution of IRNB in organs and infected sites, test mice were sacrificed at days 1, 3, 7 and 28 and the fluorescence signals were monitored by *ex vivo* fluorescent imaging. As shown in Figure 8g, h, IRNB accumulated at the infected site and decreased gradually over time. Furthermore, IRNB was also distributed in the liver and lungs, which could be attributed to phagocytosis of the reticuloendothelial system [67,68].

Antibacterial activities *in vivo* and wound healing study

The antibacterial efficiency of IRNB was examined on subcutaneous abscess and cutaneous infected wound model. Following the formation of subcutaneous abscesses or infected wounds, infected sites were locally inoculated with 100 μL PBS (100 μg/mL), BNN6-PEG (100 μg/mL), IR-780-PEG (100 μg/mL), IRN (100 μg/mL), IRNB (100 μg/mL) and IRNB (200 μg/mL), respectively, and the infected tissues were irradiated with an 808 nm laser (0.75 W/cm², 10 min) at 6 h post-inoculation.

As shown in Figure 9a, after 10 days, the mice in the IRNB (200 μg/mL) + laser group presented no apparent abscess on the dorsal side, whereas subcutaneous abscesses were still observed in the other control groups. Furthermore, the mice were sacrificed and the subcutaneous abscess tissues were homogenized followed by spreading on agar plates and colony counting. The CFU counts were then normalized and presented as percentages of those in the PBS control group. As shown in Figure 9b, c, the PBS, BNN6-PEG, IR-780-PEG, IRN, IRNB, TG, PBS + laser and BNN6-PEG + laser could not kill the bacteria within the abscesses. In contrast, the bacterial viabilities of the IR-780-PEG + laser and IRN + laser treatment groups were 85.79% ± 1.99% and 65.30% ± 3.90%, which may be attributed to nonspecific aggregation of nanomaterials in the abscesses. However, the bacterial viabilities of the IRNB (100 μg/mL) + laser group and IRNB (200 μg/mL) + laser group were 40.22% ± 3.59% and 4.60% ± 0.52%, respectively. Additionally, to further

evaluate the abscess eradication ability of IRNB, the infected tissues of all the groups were excised for histological analysis. As shown in Figure 9d, only the IRNB (200 μg/mL) + laser group presented morphological changes similar to normal skin and regression in inflammatory cells; whereas different levels of tissue destruction and inflammatory cell infiltration were evident in other groups.

As shown in Figure 10a, b, same size dorsal full-thickness excisional wounds were created and inoculated with MDR *Pa* on day 0, and different treatments were carried out on day 1. On day 3, dry and clean wounds were found in the IRNB + laser group. In contrast, various degrees of swelling and purulent exudation were found in other groups. On day 5, scabs occurred in the IRNB + laser group while purulent exudates were observed in other groups. On day 9, the wounds were almost entirely healed in the IRNB + laser group. The wound healing rates of the PBS, BNN6-PEG, IR-780-PEG, IRN, IRNB, PBS + laser, BNN6-PEG + laser, IR-780-PEG + laser, IRN + laser and IRNB + laser groups were 62.02% ± 10.03%, 63.16% ± 7.94%, 62.67% ± 8.42%, 63.13% ± 4.87%, 64.32% ± 7.24%, 60.14% ± 10.23%, 62.69% ± 10.27%, 73.17% ± 2.24%, 81.76% ± 4.30% and 94.87% ± 1.35%, respectively. The results indicated that NIR laser-triggered IRNB had an excellent therapeutic effect on MDR gram-negative bacteria infected wounds. Moreover, the infectious wounds were excised and homogenized, followed by spreading on agar plates and colony counting. As shown in Figure 10c, d, the bacterial viabilities of the BNN6-PEG, IR-780-PEG, IRN, IRNB and BNN6-PEG + laser groups were similar to the controls ($P > 0.05$). In contrast, bacterial viabilities drastically decreased to ~70%, ~40% and ~5% in the IR-780-PEG + laser, IRN + laser and IRNB + laser groups, respectively. Furthermore, the histological analysis by HE and Masson's trichromatic staining were also conducted. As shown in Figure 10e, f, the IRNB + laser group presented relatively normal skin histological structures and reduced inflammatory cell infiltration, and the new epidermis length was notably longer than the other control groups. As shown in Figure 10g, h, a substantial amount of collagen was deposited in the IRNB + laser-treated wound, suggesting the ideal formation of dermis at the infected site.

To further explore the angiogenesis ability and anti-inflammatory effect of IRNB in infectious wound healing, the expression of CD31, TNF-α and IL-6 were analyzed via immunofluorescence staining. As shown in Figure 11a, d, robust angiogenesis (as represented by CD31) were observed in the infected wounds of the control groups (the number of vessels in the PBS + laser, BNN6-PEG + laser, IR-780-PEG + laser and IRN + laser-treated groups were 40.00 ± 2.00, 37.33 ± 2.51, 32.00 ± 2.65 and 14.00 ± 2.65, respectively), whereas substantial neocapillaries were pruned back to the normal density in the IRNB + laser group (the number of vessels: 8.00 ± 2.00). As shown in Figure 11b, c, substantial TNF-α and IL-6-positive cells were observed in the wounds of the PBS + laser, BNN6-PEG + laser and IR-780-PEG + laser groups, whereas TNF-α and IL-6-positive cells were
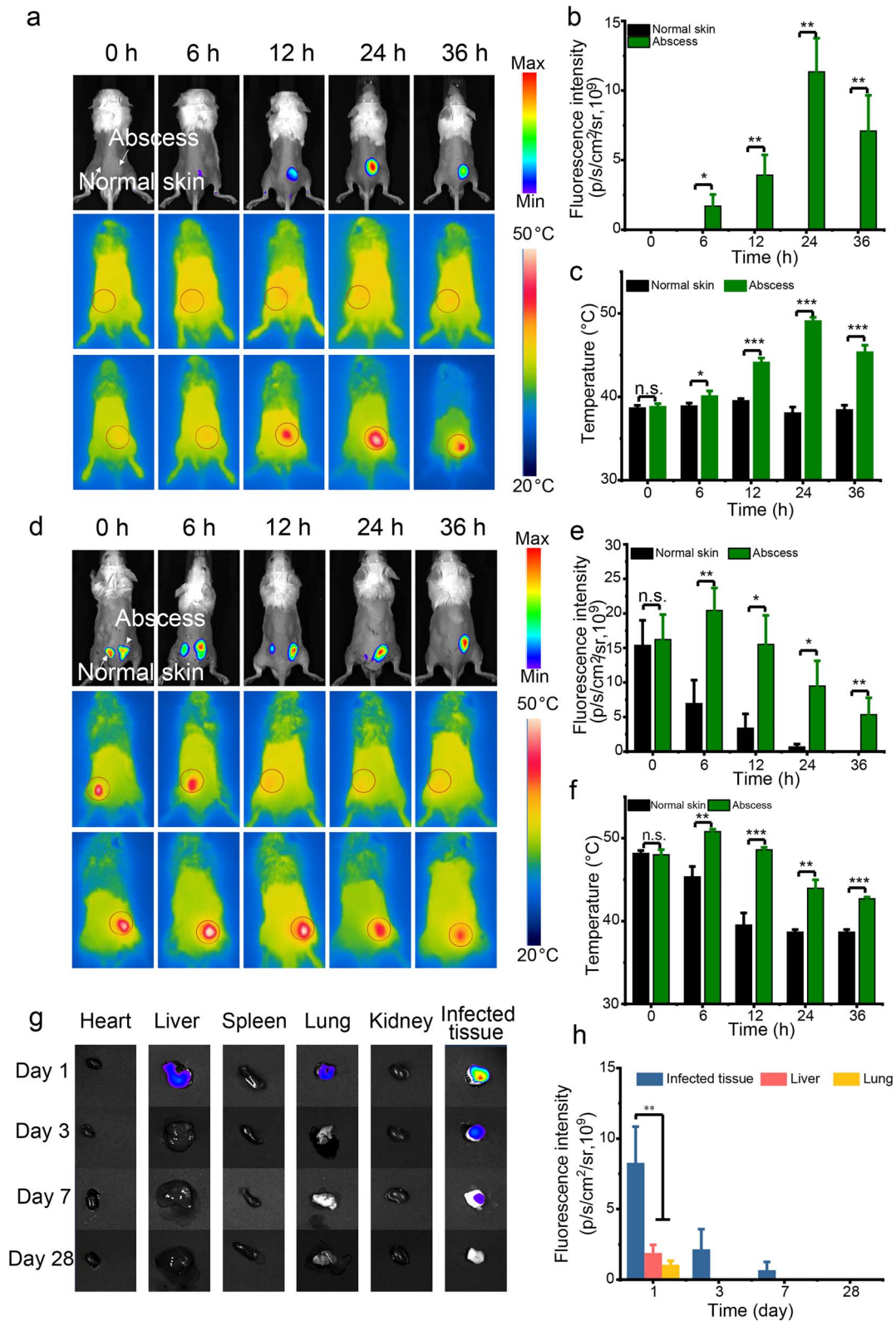
Figure 8. *In vivo* biodistribution of IRNB. (**a**) Fluorescence images and thermographic images, (**b**) the corresponding fluorescence signal intensities and (**c**) temperature measurements of the mice with abscesses after intravenous injection with IRNB at 0, 6, 12, 24 and 36 h posttreatment. (**d**) Fluorescence images and thermographic images, (**e**) the corresponding fluorescence signal intensities and (**f**) temperature measurements of the mice with abscesses after local injection with IRNB at 0, 6, 12, 24 and 36 h posttreatment. (**g**) Fluorescence images and the corresponding (**h**) fluorescence signal intensities of the heart, liver, spleen, lung, kidney and the infected wound tissue extracted from the test mice intravenously injected with IRNB at the indicated time points (days 1, 3, 7, 28) post injection. Statistical analysis: Mean ± SD; n = 3; ∗∗∗$p < 0.001$, ∗∗$p < 0.01$, ∗$p < 0.05$. *IRNB* IR-780/BNN6-PEG-PBA, *Max* maximal, *Min* minimal, *h* hour
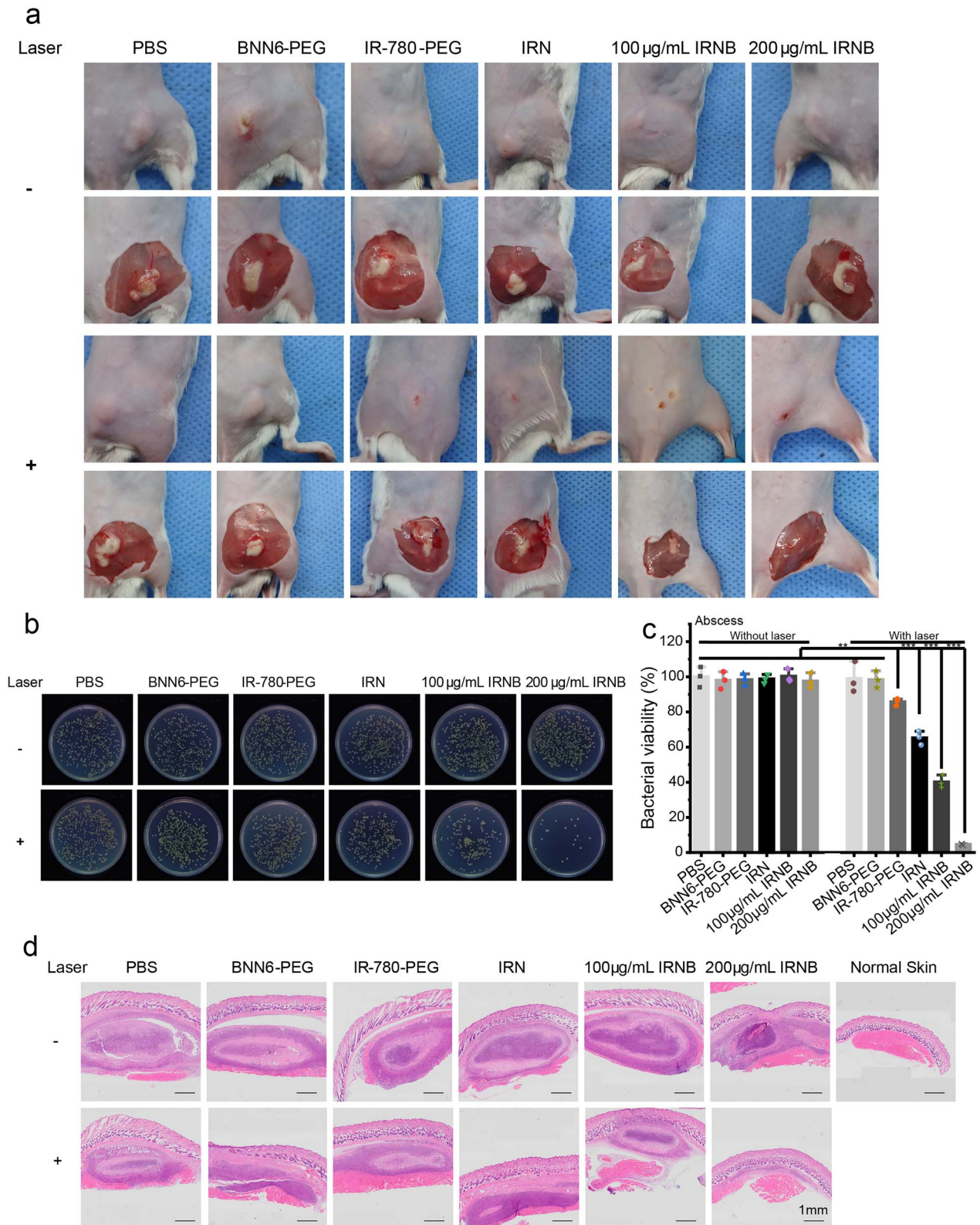
Figure 9. Effect of IRNB on the healing of subcutaneous abscess model. (**a**) Representative macroscopic appearances and biopsied photographs of the abscesses from the PBS, IR-780-PEG, BNN6-PEG, IRN, 100 μg/mL IRNB and 200 μg/mL IRNB with or without laser irradiation groups after 10 days. (**b**) Representative photographs of bacterial CFUs and (**c**) corresponding quantitative results under various treatments. (**d**) Representative H&E staining images of abscesses that received various treatments (Scale bar:1 mm). Statistical analysis: Mean $\pm$ SD; n = 3; ∗∗∗$p < 0.001$, ∗∗$p < 0.01$, ∗$p < 0.05$. *IRNB* IR-780/BNN6-PEG-PBA, *PBS* phosphate-buffered saline, *BNN6* N,N′-di-sec-butyl-N,N′- dinitroso-1,4-phenylenediamine, *IRN* IR-780/BNN6-PEG, *CFU* colony forming unit, *H&E* hematoxylin and eosin
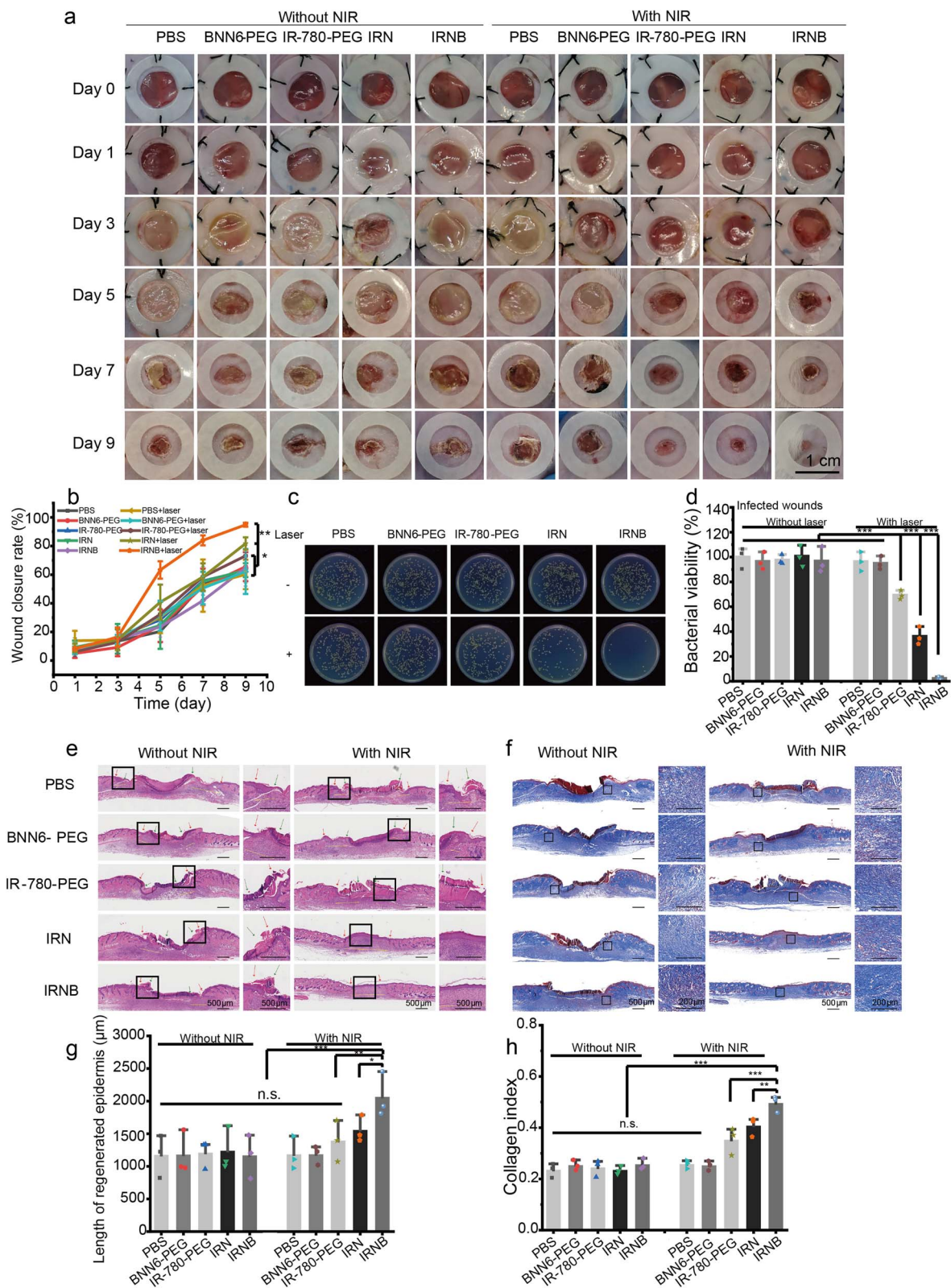
Figure 10. Effect of IRNB on the healing of cutaneous infected wound model. (**a**) Representative macroscopic appearances of the wounds from the PBS, IR-780-PEG, BNN6-PEG, IRN and IRNB with or without laser irradiation groups. (**b**) The wound closure rates at different time points. (**c**) Representative images of bacterial CFUs from the wounds and (**d**) the corresponding bacterial viabilities. (**e**) and (**f**) Representative H&E staining and Masson staining images of infected skin wounds that received various treatments on day 9 (red arrows indicate wound edges; green arrows indicate tips of epithelial tongues; yellow lines indicate the regenerated epidermis; Scale bar: 500 μm and 200 μm). (**g**) and (**h**) Quantitative determination of the length of regenerated epidermis and collagen index on day 9. Statistical analysis: Mean ± SD; n = 3; ∗∗∗$p < 0.001$, ∗∗$p < 0.01$, ∗$p < 0.05$. *IRNB* IR-780/BNN6-PEG-PBA, *PBS* phosphate-buffered saline, *BNN6* N,N′-di-sec-butyl-N,N′-dinitroso-1,4-phenylenediamine, *IRN* IR-780/BNN6-PEG, *CFU* colony forming unit, *H&E* hematoxylin and eosin

rarely observed in the IRNB + laser group, which were similar to normal skin. Specifically, as shown in Figure 11e, f, the relative fluorescent intensities of TNF-α and IL-6 in the PBS + laser, BNN6-PEG + laser, IR-780-PEG + laser, IRN + laser, IRNB + laser and normal skin groups were $100.00\% \pm 12.6\%$, $100\% \pm 7.35\%$, $99.76\% \pm 12.27\%$, $98.79\% \pm 4.98\%$, $69.17\% \pm 11.56\%$, $67.60\% \pm 3.83\%$, $50.71\% \pm 2.14\%$, $51.02\% \pm 5.53\%$, $35.60\% \pm 1.22\%$, $40.81\% \pm 2.63\%$, $25.27\% \pm 4.67\%$ and $13.78\% \pm 2.66\%$ ($P < 0.05$), respectively.

In vitro and *in vivo* biocompatibility

It is very important to evaluate the biocompatibility of INRB for future applications. A CCK-8 assay and Calcein/PI cytotoxicity assay were first performed on 3T3 fibroblasts to detect the *in vitro* cytotoxicity of IRNB. As shown in Figure 12a, b, almost all cells were alive after coincubation with IRNB (50, 100 and 500 μg/mL) for 48 h and 72 h. Moreover, cell viabilities did not change significantly after coincubation with IRNB (50 and 100 μg/mL) for 48 h and 72 h, respectively. However, the cell viabilities of the 500 μg/mL IRNB group decreased by 16% and 21% at 48 h and 72 h after coincubation, respectively. In addition, the hemocompatibility of IRNB was also investigated by a hemolysis test. As shown in Figure 12c, after incubation with IRNB (50, 100 and 500 μg/mL) for 3 h, photos of the test revealed no evident hemolysis of murine erythrocytes, and the positive control group exhibited complete hemolysis. Moreover, the hemolysis ratio was ~10% at high concentration of 500 μg/mL.

Next, the *in vivo* potential toxicity of IRNB was investigated. As shown in Figure 12d, no obvious pathological abnormalities in the heart, liver, spleen, lungor kidney were observed at 9 days after intravenous injection of IRNB (50, 100 and 500 μg/mL). Furthermore, as shown in Supplementary Figure S6, routine examination of the blood (white blood cells, red blood cells, blood platelets and hemoglobin), liver function indicators (alanine transaminase, aspartate transaminase and albumin), kidney function indicators (urea nitrogen, creatinine and uric acid) and cardiac enzymes (creatine kinase and creatine kinase isoenzyme MB) were investigated and were within the normal reference ranges, suggesting that IRNB caused no apparent impairment to the hematopoietic, hepatic, renal or cardiovascular systems.

Discussion

This study developed a novel nanoassembly IRNB composed of IR-780, BNN6, lecithin and DSPE-PEG-PBA. IRNB exhibited a synergistic antibacterial effect against MDR gram-negative bacteria and promoted healing of cutaneous infected wounds.

IRNB NPs were monodispersed, spherical in morphology, and well-dispersed in water. IRNB NPs possessed relatively high colloidal stability in various biological media. The *in vitro* release results of IR-780 and BNN6 demonstrated the controllability of IRNB release behaviors with or without laser illumination. Upon irradiation of an 808 nm NIR laser, IRNB NPs generate hyperthermia, ROS, NO and RNS in a controllable manner, making it a promising option for biomedical applications. Owing to the large amounts of LPS in gram-negative bacteria cell walls, IRNB can effectively target bacteria and produce more ROS and NO compared with the control groups via *in situ* imaging, which was consistent with previous study [69].

Hyperthermia, ROS, NO and RNS are broad-spectrum antibacterial candidates based on the destruction of bacterial cell structure, denaturation of components, lipid peroxidation, DNA breaks and protein dysfunction [15,70]. Thus, the antibacterial and antibiofilm properties of IRNB were first investigated *in vitro*. Bacterial viabilities of the IRNB-treated groups were $0.52\% \pm 0.19\%$, $1.74\% \pm 0.62\%$ and $2.96\% \pm 0.45\%$ for planktonic MDR *Ab*, *Kp* and *Pa*, respectively. In addition, IRNB could eradicate ~95% of bacterial biofilms. Overall, our findings suggest that upon illumination with an 808 nm laser, IR-780 was activated and produced ROS, thereby exerting a photothermal effect. Meanwhile, local hyperthermia could cleave thermosensitive BNN6 to generate NO gas, and further react with ROS to generate ONOO$^-$, thus enhancing the structural and functional damage to bacterial cell walls and their intercellular contents [69,71]. Notably, ROS, NO and ONOO$^-$ would place the bacteria in an extremely susceptible state. These susceptible bacteria were more vulnerable to the surrounding hyperthermal pressure. In other words, the photothermal effect was enhanced. Therefore, IRNB exerted antimicrobial effects via irreversible cell wall damage and disruption of cytoplasmic contents.

To explore whether IRNB could gather at the site of bacterial infection, both *in vivo* fluorescence imaging and thermal imaging were implemented. The results suggested that IRNB can specifically target and accumulate at the infected sites *in vivo*. Then the therapeutic effect of IRNB was examined on subcutaneous abscess and a cutaneous infected wound model. IRNB demonstrated considerable anti-abscess and anti-infected wound activity with ~90% reduction in bacterial viability. Furthermore, HE and Masson's trichromatic staining presented morphological changes similar to normal skin, regression in inflammatory cells and substantial collagen deposited in the IRNB + laser-treated groups, suggesting an ideal restoration of cutaneous integrity at the infected sites.

To further explore the angiogenesis ability and anti-inflammatory effect of IRNB in infectious wound healing, the expression of CD31, TNF-α and IL-6 were analyzed via immunofluorescence staining. Substantial neocapillaries were pruned back to the normal density in the IRNB + laser groups compared to the controls. It is known that capillary densities of wounds increase and reach 3–10 times more than normal skin tissue in the proliferative phase. However, these new capillaries are abnormal in their structure and function, as they present high tortuosity, high vascular permeability
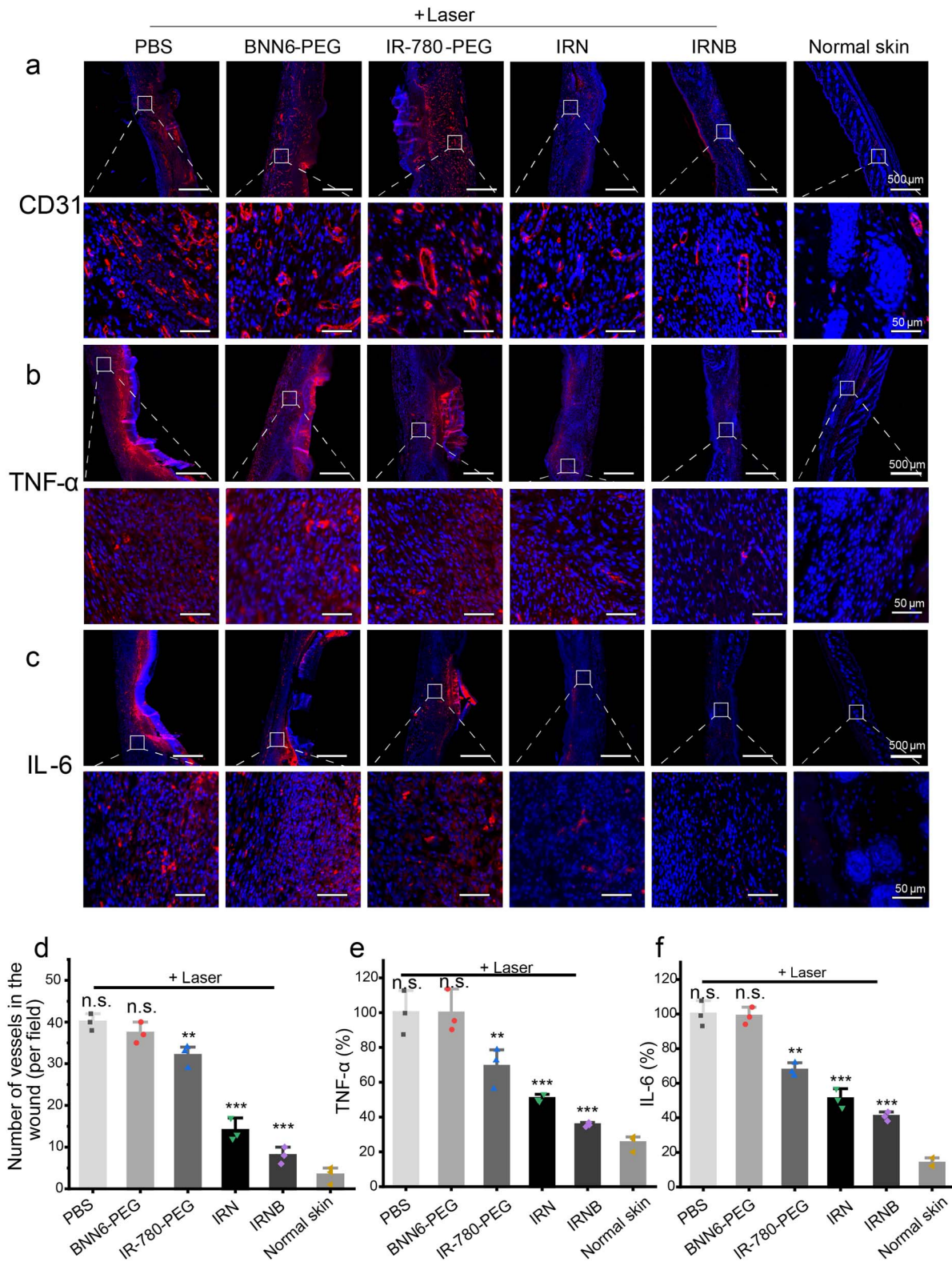
Figure 11. Evaluation of wound healing treated with IRNB by immunofluorescence. (**a**), (**b**) and (**c**) Representative confocal images of CD31, TNF-α and IL-6 in PBS, IR-780-PEG, BNN6-PEG, IRN and IRNB with laser irradiation treatment groups and normal skin on day 9 (Scale bar: 500 μm and 50 μm). (**d**), (**e**) and (**f**) Quantification of CD31, TNF-α and IL-6 in different treatment groups on day 9. Statistical analysis: Mean $\pm$ SD; n = 3; ∗∗∗$p < 0.001$, ∗∗$p < 0.01$, ∗$p < 0.05$. *IRNB* IR-780/BNN6-PEG-PBA, *PBS* phosphate-buffered saline, *BNN6* N,N′-di-sec-butyl-N,N′- dinitroso-1,4-phenylenediamine, *IRN* IR-780/BNN6-PEG, *CD31* platelet endothelial cell adhesion molecule-1, *TNF-α* tumor necrosis factor-α, *IL-6* interleukin-6, *NIR* near infrared laser
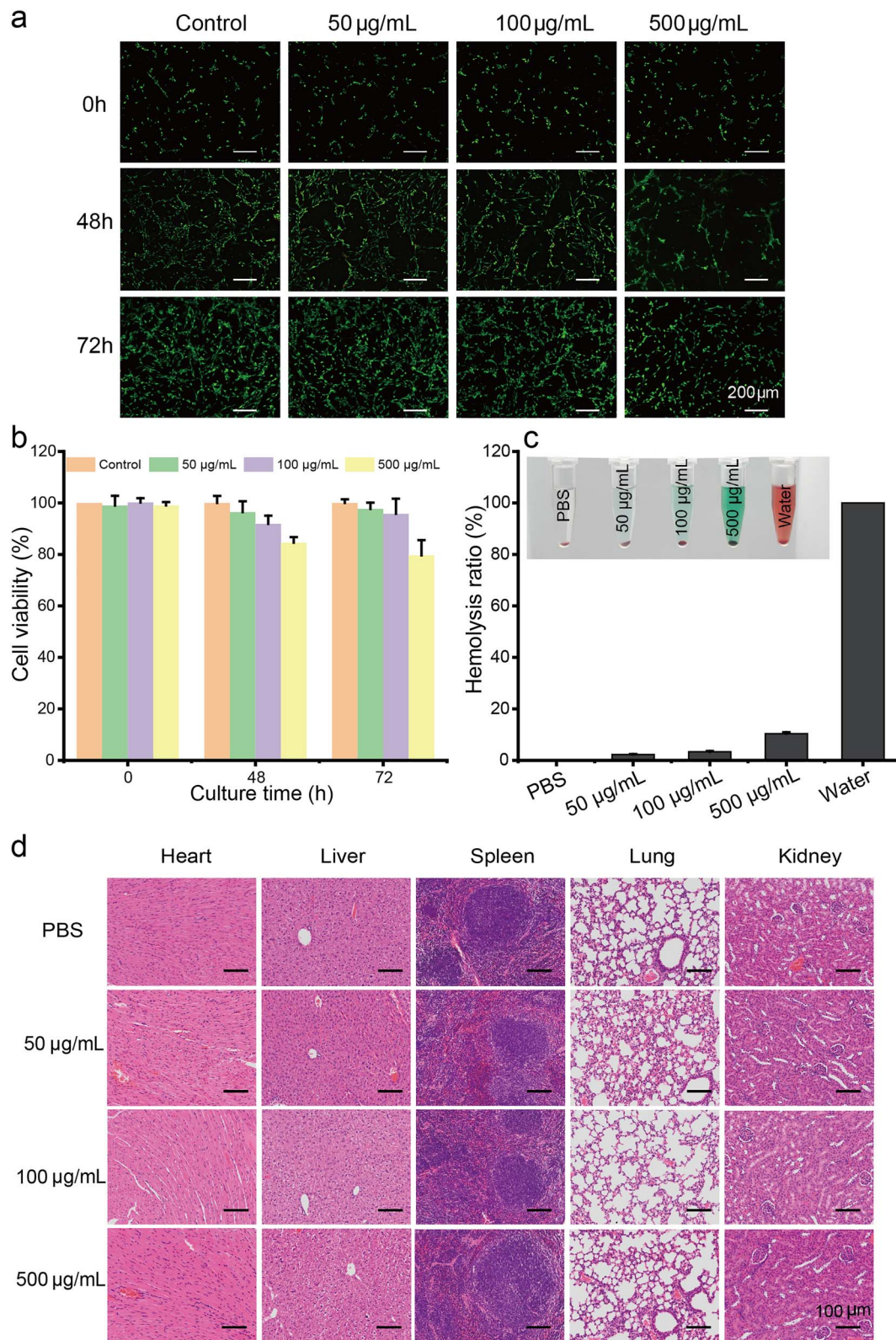
Figure 12. *In vitro* and *in vivo* biocompatibility of IRNB. (**a**) Live/dead staining of 3T3 fibroblasts after incubation with various concentrations of IRNB at the indicated time points *in vitro* (Scale bar: 200 μm). (**b**) 3T3 fibroblast viabilities treated with various concentrations of IRNB at the indicated time points *in vitro*. (**c**) Hemocompatibilities of IRNB at different concentrations. (**d**) *In vivo* toxicity evaluation of IRNB in major organs (heart, liver, spleen, lung and kidney) on day 9. (Scale bar: 100 μm). *IRNB* IR-780/BNN6-PEGPBA, *PBS* phosphate-buffered saline, *h* hour

and hemodynamic alteration. In the remodeling phase, most vessels are pruned and residual vessels mature under the regulation of antiangiogenic molecules [72,73]. Therefore, it is easy to understand that the least number of vessels were found in the IRNB + laser group in the remodeling phase after treatment. In other words, the persistent infection and inflammatory environment of the control groups may have hampered the regression of neovessels in our present study. TNF-α and IL-6 are biological cytokines that play important roles in the inflammatory response. Immunofluorescence staining results revealed that TNF-α and IL-6-positive cells were rarely observed in the IRNB + laser group, which were similar to normal skin. Taken together, these results suggested that IRNB-based synergistic therapy was quite powerful to control infection, relieve inflammation and regulate re-epithelization, collagen deposition and angiogenesis in MDR gram-negative bacteria infected wounds.

It is very important to evaluate the biocompatibility of INRB for future applications. A CCK-8 assay, Calcein/PI cytotoxicity assay, and a hemolysis test were performed to detect the *in vitro* cytotoxicity of IRNB. The results revealed that IRNB could be considered to have no or negligible cytotoxic potential at concentrations <500 μg/mL according to the International Standard ISO 10993-5: 2009 and American Society for Testing and Materials (ASTM F756–93, [74,75]. *In vivo* potential toxicity experiments indicated that IRNB caused negligible influence on the structures of the internal organs and no apparent impairment to the hematopoietic, hepatic, renal or cardiovascular systems. Overall, the above findings suggested that IRNB exhibited good biocompatibility both *in vitro* and *in vivo* and could be highly suitable for biomedical applications.

Currently, researches have been carried out on PTT/PDT/NO-based antimicrobial nanotherapies. In contrast with previous research, the present study has these innovative following points. First, unlike other nanomaterials (e.g. MXene [76], metal nanoparticles [62], and metal–organic framework [66]), the one-pot preparation procedure of IRNB is simple with mild reaction conditions, which is suitable for large-scale production. Second, the outer layer nanoassembly of IRNB was wrapped by lecithin and DSPE-PEG, and further decorated with PBA. The outer layer enhances biocompatibility, prolongs circulation time and increases infection-targeting efficacy. Third, compared with other passive targeting stimuli-responsive (e.g. pH [45], enzyme [42]) nanomaterials, the PBA ligand of IRNB actively conjugated with bacteria and their biofilms, thus minimizing damage to surrounding normal tissues and achieving robust bactericidal efficiency [46,74]. Upon irradiation using an 808 nm laser, IRNB is activated and produces both ROS and hyperthermia. Local hyperthermia can in turn induce the generation of NO, and further react with ROS to generate ONOO$^-$, thereby enhancing bactericidal efficacy [42]. Furthermore, the generated ROS, NO and ONOO$^-$ can disrupt the cell membrane, which convert the bacteria to an extremely susceptible state, and enhance the photothermal effect. In addition to effectively controlling MDR gram-negative bacteria and biofilm-associated subcutaneous and wound infections, IRNB-based synergistic therapy can also relieve inflammation, promote re-epithelization and collagen deposition, and regulate angiogenesis during wound healing. Finally, the inherent fluorescent nature of IRNB makes it simple and convenient for exploring and tracking the biodistribution using fluorescent imaging both *in vitro* and *in vivo*.

Conclusions

In summary, we have successfully developed a multifunctional nanoassembly (IRNB) based on IR-780 and BNN6 for synergistic PTT, PDT and NO effects triggered by an 808 nm NIR laser. This bactericidal nanosystem could specifically accumulate at the infected sites of MDR gram-negative bacteria by a covalent effect, showing a superior photothermal-photodynamic-chemo (NO) synergistic therapeutic efficacy toward infected wounds and subcutaneous abscesses. This led to efficient control of associated infections, relief of inflammation, promotion of re-epithelization and collagen deposition, and regulation of angiogenesis during wound healing. Finally, IRNB showed good biocompatibility both *in vitro* and *in vivo*. Therefore, we conclude that the IRNB system developed in this study can be considered a novel and promising option against MDR gram-negative bacteria-mediated infections.

Abbreviations

Ab: *Acinetobacter baumannii*; BA: Boronic acid; BNN6: *N,N'*-di-sec-butyl-*N,N'*- dinitroso-1,4-phenylenediamine; CCK-8: Cell counting kit 8; CD31: Platelet endothelial cell adhesion molecule-1; CFU: Colony forming unit; CLSM: Confocal laser scanning microscopy; CH_3CN: Acetonitrile; CV: Crystal violet; DAF-FM DA: 4-Amino-5-methylamino-2′,7′-difluorofluorescein diacetate; DCFH-DA: 2′,7'-Dichlorodihydrofluorescein diacetate; DHR 123: Dihydrorhodamine 123; DI water: Deionized water; DLS: Dynamic light scattering; DMEM: Dulbecco's Modified Eagle Medium; DPBF: 1,3-diphenylisobenzofuran; DSPE-PEG-PBA: 1,2-distearoyl-sn-glycero-3-phosphoethanolamine-N-[methoxy(polyethylene glycol)-2000]-phenylboronic acid; FBS: Fetal bovine serum; FTIR: Fourier transform infrared spectroscopy; H&E: Hematoxylin and eosin; IL-6: Interleukin-6; IRN: IR-780/BNN6-PEG, IRNB: IR-780/BNN6-PEG-PBA; LB: Luria–Bertani; *Kp*: *Klebsiella pneumoniae*; MDR: multidrug-resistant; MWCO: molecular weight cut-off; NIR: Near infrared; NO: Nitric oxide; *Pa*: *Pseudomonas aeruginosa*; OD: Optical density; PBA: Phenylboronic acid; PBS: Phosphate-buffered saline; PDT: Photodynamic therapy; PTT: Photothermal therapy; RNS: Reactive nitrogen species; ROS: Reactive oxygen species; SEM: Scanning electron microscopy; TEM: Transmission electron microscopy; TNF-α: Tumor necrosis factor-α

Supplementary material

Supplementary material is available at *BURNST Journal* online.

Funding

Authors' contributions

XZ, LD: Investigation, Formal analysis, Data curation, Visualization, Writing Original Draft. BZ, CH, GH: Investigation, Writing—Review and Editing. TL, YL: Investigation. MZ, ZY, YY: Writing—Review and Editing. YX, SC, GL: Resources, Software. WQ, RY: Project administration, Supervision, Funding acquisition.

Ethics approval

All animal experimental procedures were approved by the Animal Ethics Committee of Third Military Medical University (Number: AMUWEC20201405).

Conflict of interest

None declared.

Data availability statement

All data or related information supporting the conclusions of the study is included in the article.

References

1. Mccann E, Srinivasan A, Deryke CA, Ye G, Depestel DD, Murray J, *et al.* Carbapenem-nonsusceptible gram-negative pathogens in ICU and non-ICU settings in US hospitals in 2017: a Multicenter study. *Open Forum Infect Di*. 2018;5:ofy241.

2. Centers for Disease Control and Prevention (U.S.). *Antibiotic resistance threats in the United States*. 2019;2019. https://doi.org/10.15620/cdc:82532.

3. Falcone M, Paterson D. Spotlight on ceftazidime/avibactam: a new option for MDR gram-negative infections. *J Antimicrob Chemoth*. 2016;71:2713–22.

4. Corcione S, Lupia T, De Rosa FG. Microbiome in the setting of burn patients: implications for infections and clinical outcomes. *Burns*. *Trauma*. 2020;8:tkaa033.

5. Cook MA, Wright GD. The past, present, and future of antibiotics. *Sci Transl Med*. 2022;14:eabo7793.

6. Trubenová B, Roizman D, Moter A, Rolff J, Regoes RR. Population genetics, biofilm recalcitrance, and antibiotic resistance evolution. *Trends Microbiol*. 2022;30:841–52.

7. Martin HM, Campbell BJ, Hart CA, Mpofu C, Nayar M, Singh R, *et al.* Enhanced Escherichia coli adherence and invasion in Crohn's disease and colon cancer. *Gastroenterology*. 2004;127:80–93.

8. Banerjee D, Shivapriya PM, Gautam PK, Misra K, Sahoo AK, Samanta SK. A review on basic biology of bacterial biofilm infections and their treatments by nanotechnology-based approaches. *Proceedings of the National Academy of Sciences, India Section B: Biological Sciences*. 2020;90:243–59.

9. Dai T, Huang YY, Hamblin MR. Photodynamic therapy for localized infections–state of the art. *Photodiagn Photodyn Ther*. 2009;6:170–88.

10. Hamblin MR, Hasan T. Photodynamic therapy: a new antimicrobial approach to infectious disease? *Photoch Photobio Sci*. 2004;3:436–50.

11. Xiu W, Wan L, Yang K, Li X, Yuwen L, Dong H, *et al.* Potentiating hypoxic microenvironment for antibiotic activation by photodynamic therapy to combat bacterial biofilm infections. *Nat Commun*. 2022;13:3875.

12. Zhou J, Li M, Hou Y, Luo Z, Chen Q, Cao H, *et al.* Engineering of a nanosized biocatalyst for combined tumor starvation and low-temperature photothermal therapy. *ACS Nano*. 2018;12:2858–72.

13. Qiao Y, Ma Y, Tong Y, Liu W, Wang S, Zheng Y, *et al.* Phototherapy and mechanism exploration of biofilm and multidrug-resistant helicobacter pylori by bacteria-targeted NIR photosensitizer. *Small*. 2023;19:e2205248.

14. Liu J, Li RS, He M, Xu Z, Xu LQ, Kang Y, *et al.* Multifunctional SGQDs-CORM@HA nanosheets for bacterial eradication through cascade-activated "nanoknife" effect and photodynamic/CO gas therapy. *Biomaterials*. 2021;277: 121084.

15. Yuan Z, Lin C, He Y, Tao B, Chen M, Zhang J, *et al.* Near-infrared light-triggered nitric-oxide-enhanced photodynamic therapy and low-temperature photothermal therapy for biofilm elimination. *ACS Nano*. 2020;14:3546–62.

16. Liu X, Fang R, Feng R, Li Q, Su M, Hou C, *et al.* Cage-modified hypocrellin against multidrug-resistant Candida spp. with unprecedented activity in light-triggered combinational photodynamic therapy. *Drug resist*. *Update*. 2022;65:100887.

17. Santos P, Gomes A, Lourenco L, Faustino M, Neves M, Almeida A. Anti-viral photodynamic inactivation of T4-like bacteriophage as a mammalian virus model in blood. *Int J Mol Sci*. 2022;23:11548.

18. Ran L, Lu B, Qiu H, Zhou G, Jiang J, Hu E, *et al.* Erythrocyte membrane-camouflaged nanoworms with on-demand antibiotic release for eradicating biofilms using near-infrared irradiation. *Bioact Mater*. 2021;6:2956–68.

19. Hao S, Han H, Yang Z, Chen M, Jiang Y, Lu G, *et al.* Recent advancements on photothermal conversion and antibacterial applications over MXenes-based materials. *Nano-Micro Lett*. 2022;14:178.

20. Li J, Sun W, Yang Z, Gao G, Ran HH, Xu KF, *et al.* Rational design of self-assembled cationic porphyrin-based nanoparticles for efficient photodynamic inactivation of bacteria. *Acs Appl Mater Inter*. 2020;12:54378–86.

21. Abdel KM, Abdel GS, El-Domany RA, El-Kemary MA. Photoactive electrospun cellulose acetate/polyethylene oxide/methylene blue and trilayered cellulose acetate/polyethylene oxide/silk fibroin/ciprofloxacin nanofibers for chronic wound healing. *Int J Biol Macromol*. 2021;193Pt B:1752–66.

22. Yang X, Ye Y, Sun J, Li Z, Ping J, Sun X. Recent advances in g-C$_3$N$_4$ -based photocatalysts for pollutant degradation and bacterial disinfection: design strategies, mechanisms, and applications. *Small*. 2022;18:e2105089.

23. Cheng H, Wang J, Yang Y, Shi H, Shi J, Jiao X, *et al.* Ti$_3$C$_2$T$_X$ MXene modified with ZnTCPP with bacteria capturing capability and enhanced visible light photocatalytic antibacterial activity. *Small*. 2022;18:e2200857.

24. Huang Y, Mu L, Zhao X, Han Y, Guo B. Bacterial growth-induced tobramycin smart release self-healing hydrogel for Pseudomonas aeruginosa-infected burn wound healing. *ACS Nano*. 2022;16:13022–36.

25. Leitao MM, de Melo-Diogo D, Alves CG, Lima-Sousa R, Correia IJ. Prototypic heptamethine cyanine incorporating nanomaterials for cancer phototheragnostic. *Adv Healthc Mater*. 2020;9:e1901665.

26. Gnanasekar S, Kasi G, He X, Zhang K, Xu L, Kang ET. Recent advances in engineered polymeric materials for efficient photodynamic inactivation of bacterial pathogens. *Bioact Mater*. 2023;21:157–74.

27. Zhang L, Yang J, Zhu X, Jia X, Liu Y, Cai L, *et al.* Electrospun nanofibrous membranes loaded with IR780 conjugated MoS2-nanosheet for dual-mode photodynamic/photothermal inactivation of drug-resistant bacteria. *Environ Technol Inno*. 2023;30:103098.

28. Gao D, Shi Y, Ni J, Chen S, Wang Y, Zhao B, *et al.* NIR/MRI-guided oxygen-independent carrier-free anti-tumor nano-theranostics. *Small*. 2022;18:e2106000.

29. Roemhild R, Bollenbach T, Andersson DI. The physiology and genetics of bacterial responses to antibiotic combinations. *Nat Rev Microbiol*. 2022;20:478–90.

30. Beurton J, Boudier A, Barozzi SA, Vrana NE, Clarot I, Lavalle P. Nitric oxide delivering surfaces: an overview of functionalization strategies and efficiency progress. *Adv Healthc Mater*. 2022;11:2102692.

31. Zhou B, Sun X, Dong B, Yu S, Cheng L, Hu S, *et al.* Antibacterial PDT nanoplatform capable of releasing therapeutic gas for synergistic and enhanced treatment against deep infections. *Theranostics*. 2022;12:2580–97.

32. Liu FT, Li N, Chen YS, Yu HY, Miao JY, Zhao BX. A quinoline-coumarin near-infrared ratiometric fluorescent probe for detection of sulfur dioxide derivatives. *Anal Chim Acta*. 2022;1211:339908.

33. Han L, Liu XW, Zang T, Ren H, Liang DS, Bai SC, *et al.* H_2S responsive PEGylated poly (lipoic acid) with ciprofloxacin for targeted therapy of salmonella. *J Control Release*. 2022;351:896–906.

34. Zhang W, Zhou Y, Fan Y, Cao R, Xu Y, Weng Z, *et al.* Metal-organic-framework-based hydrogen-release platform for multieffective helicobacter pylori targeting therapy and intestinal flora protective capabilities. *Adv Mater*. 2022;34:e2105738.

35. Rong F, Tang Y, Wang T, Feng T, Song J, Li P, *et al.* Nitric oxide-releasing polymeric materials for antimicrobial applications: a review. *Antioxidants-Basel*. 2019;8:556.

36. Juedes MJ, Wogan GN. Peroxynitrite-induced mutation spectra of pSP189 following replication in bacteria and in human cells. *Mutat Res-Fund Mol M*. 1996;3491:51–61.

37. Kresnajati S, Lin YY, Mundel T, Bernard JR, Lin HF, Liao YH. Changes in arterial stiffness in response to various types of exercise modalities: a narrative review on physiological and endothelial senescence perspectives. *Cells-Basel*. 2022;11:3544.

38. Suvorava T, Metry S, Pick S, Kojda G. Alterations in endothelial nitric oxide synthase activity and their relevance to blood pressure. *Biochem Pharmacol*. 2022;205:115256.

39. Xie W, Hu W, Huang Z, Li M, Zhang H, Huang X, *et al.* Betulinic acid accelerates diabetic wound healing by modulating hyperglycemia-induced oxidative stress, inflammation and glucose intolerance. *Burns Trauma*. 2022;10:tkac007.

40. Szabo C, Ischiropoulos H, Radi R. Peroxynitrite: biochemistry, pathophysiology and development of therapeutics. *Nat Rev Drug Discov*. 2007;6:662–80.

41. Deng Y, Jia F, Chen S, Shen Z, Jin Q, Fu G, *et al.* Nitric oxide as an all-rounder for enhanced photodynamic therapy: hypoxia relief, glutathione depletion and reactive nitrogen species generation. *Biomaterials*. 2018;187:55–65.

42. Hu D, Deng Y, Jia F, Jin Q, Ji J. Surface charge switchable supramolecular nanocarriers for nitric oxide synergistic photodynamic eradication of biofilms. *ACS Nano*. 2020;14:347–59.

43. Zhan R, Wang F, Wu Y, Wang Y, Qian W, Liu M, *et al.* Nitric oxide induces epidermal stem cell de-adhesion by targeting integrin beta1 and Talin via the cGMP signalling pathway. *Nitric Oxide-Biol Ch*. 2018;78:1–10.

44. Lu B, Hu E, Xie R, Yu K, Lu F, Bao R, *et al.* Magnetically guided nanoworms for precise delivery to enhance in situ production of nitric oxide to combat focal bacterial infection in vivo. *Acs Appl Mater Inter*. 2021;13:22225–39.

45. Zhang L, Zhang L, Deng H, Li H, Tang W, Guan L, *et al.* In vivo activation of pH-responsive oxidase-like graphitic nanozymes for selective killing of helicobacter pylori. *Nat Commun*. 2021;12:2002.

46. Chen M, Zhang J, Qi J, Dong R, Liu H, Wu D, *et al.* Boronic acid-decorated multivariate photosensitive metal-organic frameworks for combating multi-drug-resistant bacteria. *ACS Nano*. 2022;16:7732–44.

47. Ling C, Yanqiang H, Yuanyuan D, Qiao L, Qilan X, Jia J, *et al.* Schiff-base silver nanocomplexes formation on natural biopolymer coated mesoporous silica contributed to the improved curative effect on infectious microbes. *Nano Res*. 2021;14:2735–48.

48. Song Y, Cai L, Tian Z, Wu Y, Chen J. Phytochemical curcumin-coformulated, silver-decorated melanin-like polydopamine/mesoporous silica composites with improved antibacterial and chemotherapeutic effects against drug-resistant cancer cells. *Acs Omega*. 2020;5:15083–94.

49. Deng Q, Sun P, Zhang L, Liu Z, Wang H, Ren J, *et al.* Porphyrin MOF dots–based, function-adaptive nanoplatform for enhanced penetration and photodynamic eradication of bacterial biofilms. *Adv Funct Mater*. 2019;29:1903018.

50. Cai L, Zhu X, Ruan H, Yang J, Wei W, Wu Y, *et al.* Curcumin-stabilized silver nanoparticles encapsulated in biocompatible electrospun nanofibrous scaffold for sustained eradication of drug-resistant bacteria. *J Hazard Mater*. 2023;452:131290.

51. Xiao YF, An FF, Chen JX, Yu J, Tao WW, Yu Z, *et al.* The nanoassembly of an intrinsically cytotoxic near-infrared dye for multifunctionally synergistic theranostics. *Small*. 2019;15:e1903121.

52. Cun J, Pan Y, Zhang Z, Lu Y, Li J, Pan Q, *et al.* Photo-enhanced upcycling H_2O_2 into hydroxyl radicals by IR780-embedded Fe3O4@MIL-100 for intense nanocatalytic tumor therapy. *Biomaterials*. 2022;287:121687.

53. Li M, Li L, Su K, Liu X, Zhang T, Liang Y, *et al.* Highly effective and noninvasive near-infrared eradication of a staphylococcus aureus biofilm on implants by a photoresponsive coating within 20 min. *Adv Sci*. 2019;6:1900599.

54. Wang S, Liu Z, Tong Y, Zhai Y, Zhao X, Yue X, *et al.* Improved cancer phototheranostic efficacy of hydrophobic IR780 via parenteral route by association with tetrahedral nanostructured DNA. *J Control Release*. 2021;330:483–92.

55. Tan Y, Li Y, Huang J, Luo M, Li S, Lee AW, *et al.* Thermal-sensitive lipid nanoparticles potentiate anti-PD therapy through enhancing drug penetration and T lymphocytes infiltration in metastatic tumor. *Cancer Lett*. 2021;522:238–54.

56. Ren W, Yan Y, Zeng L, Shi Z, Gong A, Schaaf P, *et al.* A near infrared light triggered hydrogenated black TiO_2 for cancer photothermal therapy. *Adv Healthc Mater*. 2015;4:1526–36.

57. Saravanakumar G, Park H, Kim J, Park D, Lim J, Lee J, *et al*. Polymersomes with singlet oxygen-labile poly(β-aminoacrylate) membrane for NIR light-controlled combined chemo-phototherapy. *J Control Release*. 2020;327: 627–40.

58. Xue P, Hou M, Sun L, Li Q, Zhang L, Xu Z, *et al*. Calcium-carbonate packaging magnetic polydopamine nanoparticles loaded with indocyanine green for near-infrared induced photothermal/photodynamic therapy. *Acta Biomater*. 2018;81: 242–55.

59. Huang S, Liu H, Liao K, Hu Q, Guo R, Deng K. Functionalized GO nanovehicles with nitric oxide release and photothermal activity-based hydrogels for bacteria-infected wound healing. *Acs Appl Mater Inter*. 2020;1226:28952–64.

60. Gehring J, Trepka B, Klinkenberg N, Bronner H, Schleheck D, Polarz S. Sunlight-triggered nanoparticle synergy: teamwork of reactive oxygen species and nitric oxide released from mesoporous organosilica with advanced antibacterial activity. *J Am Chem Soc*. 2016;138:3076–84.

61. Zhang S, Cao Z, Fan P, Wang Y, Jia W, Wang L, *et al*. A nanopore-based saccharide sensor. *Angew Chem*. 2022;134:e202203769.

62. Halbus AF, Horozov TS, Paunov VN. Strongly enhanced antibacterial action of copper oxide nanoparticles with boronic acid surface functionality. *Acs Appl Mater Inter*. 2019;11:12232–43.

63. Xu Y, Chen H, Xu S, Liu J, Chen Y, Gui L, *et al*. β-Lactamase-responsive probe for efficient photodynamic therapy of drug-resistant bacterial infection. *Acs Sensors*. 2022;7:1361–71.

64. Liang Z, Liu W, Wang Z, Zheng P, Liu W, Zhao J, *et al*. Near-infrared laser-controlled nitric oxide-releasing gold nanostar/hollow polydopamine Janus nanoparticles for synergistic elimination of methicillin-resistant Staphylococcus aureus and wound healing. *Acta Biomater*. 2022;143:428–44.

65. Deng Y, Jia F, Chen X, Jin Q, Ji J. ATP suppression by pH-activated mitochondria-targeted delivery of nitric oxide nanoplatform for drug resistance reversal and metastasis inhibition. *Small*. 2020;16:e2001747.

66. Yang Y, Huang K, Wang M, Wang Q, Chang H, Liang Y, *et al*. Ubiquitination flow repressors: enhancing wound healing of infectious diabetic ulcers through stabilization of polyubiquitinated hypoxia-inducible factor-1α by theranostic nitric oxide nanogenerators. *Adv Mater*. 2021;33:e2103593.

67. Yang C, Ming Y, Zhou K, Hao Y, Hu D, Chu B, *et al*. Macrophage membrane-camouflaged shRNA and doxorubicin: a pH-dependent release system for melanoma chemo-immunotherapy. *Research-China*. 2022;2022:9768687.

68. Zhang Y, Teng Z, Ni Q, Tao J, Cao X, Wen Y, *et al*. Orderly curled silica nanosheets with a small size and macromolecular loading pores: synthesis and delivery of macromolecules to eradicate drug-resistant cancer. *Acs Appl Mater Inter*. 2020;12:57810–20.

69. Wang H, Zhao B, Dong W, Zhong Y, Zhang X, Gong Y, *et al*. A dual-targeted platform based on graphene for synergistic chemo-photothermal therapy against multidrug-resistant gram-negative bacteria and their biofilms. *Chem Eng J*. 2020;393: 124595.

70. Privett BJ, Broadnax AD, Bauman SJ, Riccio DA, Schoenfisch MH. Examination of bacterial resistance to exogenous nitric oxide. *Nitric Oxide-Biol Ch*. 2012;26:169–73.

71. Zhao Z, Li H, Tao X, Xie Y, Yang L, Mao ZW, *et al*. Light-triggered nitric oxide release by a photosensitizer to combat bacterial biofilm infections. *Chemistry – a. European Journal*. 2021;27:5453–60.

72. Jiang J, Zang J, Ru Y, Luo Y, Song J, Luo Y, *et al*. Patient-driven discovery of CCN1 to rescue cutaneous wound healing in diabetes via the intracellular EIF3A/CCN1/ATG7 signaling by nanoparticle-enabled delivery. *Biomaterials*. 2022;288:121698.

73. Han C, Barakat M, Dipietro LA. Angiogenesis in wound repair: too much of a good thing? *Csh Perspect Biol*. 2022;14:a041225.

74. Zhao B, Wang H, Dong W, Cheng S, Li H, Tan J, *et al*. A multifunctional platform with single-NIR-laser-triggered photothermal and NO release for synergistic therapy against multidrug-resistant gram-negative bacteria and their biofilms. *J Nanobiotechnol*. 2020;18:59.

75. Freedman BR, Mooney DJ. Biomaterials to mimic and heal connective tissues. *Adv Mater*. 2019;31:1806695.

76. Zheng K, Li S, Jing L, Chen PY, Xie J. Synergistic antimicrobial titanium carbide (MXene) conjugated with gold nanoclusters. *Adv Healthc Mater*. 2020;9:e2001007.